# Liquid mobility on superwettable surfaces for applications in energy and the environment

Zhang, Songnan; Huang, Jianying; Chen, Zhong; Yang, Shu; Lai, Yuekun

2018

https://hdl.handle.net/10356/143071

https://doi.org/10.1039/C8TA09403A

# Journal Name

## ARTICLE

# Liquid Mobility on Super-wettable Surfaces for Applications in Energy and Environment

Songnan Zhang,[‡ad] Jianying Huang,[‡b] Zhong Chen,[c] Shu Yang,[d] and Yuekun Lai*[b]

Liquid mobility on super-wettable materials are of interests for enhanced heat transfer, self-cleaning, anti-fouling, anti-icing, water-harvesting, and oil-water separation. Here, we review different mechanisms related to liquid mobility on super-wettable materials, encompassing some classical wetting theories and liquid transport behaviors observed on the biological surfaces with special textures. Then, a detailed account of different categories of liquid behaviors on super-wettability materials are summarized, focusing on recent progresses on vertical motion (droplet self-propelling and bouncing), horizontal transportation (transportation on one-dimensional (1-D) and two-dimensional (2-D) materials), and interfacial penetration (oil-water penetration and water penetration). Along the lines, we will review latest applications in energy and environment, followed by outlook and challenges.

## 1. Introduction

In 1805, Thomas Young first introduced liquid wetting theory on a smooth solid surface.[1] Wenzel and Cassie-Baxter then proposed theoretical models describing wetting on rough and heterogeneous surfaces in 1936 and 1944, respectively.[2-4] Subsequently, Rosano stated theoretical model of the sliding angle on a flat surface in 1951.[5] Despite of these early theories, it was not until recently that researchers started to realize that nature has produced many different types of special wettability that can be perfectly described by these theories. Barthlott found that lotus leaf possesses a special self-cleaning functionality due to the special structure and superwettability.[6] Since then, more and more creatures with special superwettability were found and investigated, such as cicada wing, butterfly wing, rice leaf, mosquito compound eyes, water strider, pitcher plant and so on.[7-12] Meanwhile, inspired by the creatures with special functionality, materials with superwettability has received extensive attention in the last two decades. Based on the special super-wettability materials, liquid mobility has been studied by a number of researchers, including vertical bouncing, horizontal transportation, and interface penetration.

Liquid mobility is a significant topic in various industrial and chemical engineering fields, including heat transfer enhancement, self-cleaning, anti-fouling, anti-icing, water-harvesting, oil-water separation, and so on. Boerhaave found that when a water droplet is dropped on a hot substrate with a very high temperature, the droplet will bounce off and roll away, because of the participation of an integral air cushion between the underlying substrate and imping droplet. This phenomenon was investigated by Leidenfrost and subsequently other researchers with the aim of controlling directional droplets bouncing, enhancing heat transfer, and increasing the critical temperature at which this phenomenon named after Leidenfrost occurs.[13] On the other hand, droplet bouncing on a substrate without heating was first systematically investigated by the Richard and his coworkers, when they studied the duration of a droplet in contact with the substrate.[14] Since then, scientists have investigated ways to decrease the contact duration of a bouncing droplet. Inspired by some special creatures, such as cicada wing, lotus leaf, shark skin etc.,[6, 7] researchers have focused their investigation on the mechanism of water droplet self-propelling, transporting on and penetrating through the surfaces with special structures. Success has been made in the fabricating smart materials for directional liquid mobility. Impressive advances have been made in bionic materials research in terms of fundamental understanding and potential applications in environmental energy fields, and human healthcare.

To understand the liquid mobility on special super-wettability materials, it is significant to comprehend its intrinsic mechanisms before investigating the phenomenon of liquid mobility. Therefore, in this review, we first cover the mechanisms of liquid wettability on surfaces, which is further divided into three parts. The first one is theories of liquid wetting on flat and rough surfaces, the second one is theory of liquid sliding on tilted surface, the third one is principles of liquid transport behaviours on biological surfaces. As for the theories of liquid wetting, we focus on three models, that is the Young's contact model, Wenzel model, Cassie model. As for the theory of liquid sliding, we focus on the Rosano model. As for the principles of liquid transport behaviours on biological surfaces, we principally review some gradients that exist on the creatures with distinct surface structural characteristics for directional liquid mobility. These include the Laplace gradient and surface energy gradient, special aligned textured surfaces.

Next, we focus on the influencing factors for different types of liquid mobility, covering vertical motion, horizontal transportation and interfacial penetration. The vertical motion is further divided into droplet self-propelling and droplet bouncing. Horizontal transportation will focus on the motion on 1-D and 2-D materials,

a. National Engineering Laboratory for Modern Silk, College of Textile and Clothing Engineering, Soochow University, Suzhou 215123, China
b. College of Chemical Engineering, Fuzhou University, Fuzhou 350116, China
c. School of Materials Science and Engineering, Nanyang Technological University, 50 Nanyang Avenue, Singapore 639798, Singapore
d. Department of Materials Science and Engineering, University of Pennsylvania, 3231 Walnut Street, Philadelphia, PA 19104, USA
†These authors contributed equally.
Corresponding Authors E-mail: yklai@suda.edu.cn

while interface penetration includes oil-water penetration and water-only penetration based on the difference of the mixture.

We then cover the mechanism of droplet mobility by looking into the surface wettability and driving force analysis. Following this, we summarize some typical applications that require special liquid mobility, including heat transfer enhancement, anti-icing, self-cleaning, antifouling, water-harvesting, and oil-water separation. Finally, we present the outlook in research of biomimetic materials with special liquid mobility.

## 2. Mechanisms of liquid wettability on surfaces

### 2.1 Theories of liquid wetting on flat and rough surfaces

Liquid contact angle is a measure of equilibrium between solid-liquid, solid-gas, and gas-liquid interfacial energies when a liquid droplet is placed on a solid surface. Herein, we present three classical theories are introduced below, that is Young's model, Wenzel's model, and Cassie's model.

**2.1.1 On a flat surface:** The basic theory of liquid contact angle on a flat surface can be described by the Young equation (Fig. 1A) proposed by Young in 1805, which describes the relationship between the static contact angle ($\theta$) of the droplet and the surface tension of three interfacial tensions (solid-liquid, solid-gas and gas-liquid) on the smooth surface:[1]

$$\cos \theta = \frac{(\gamma_{SG} - \gamma_{SL})}{\gamma_{GL}} \qquad (1)$$

where $\gamma_{SG}$, $\gamma_{SL}$, $\gamma_{GL}$ represent solid-gas, solid-liquid, gas-liquid interfacial tensions, respectively, when $\theta$ is greater than 90°, it displays hydrophobicity, otherwise hydrophilicity. This model is only suitable for physically smooth and chemically uniform surfaces. In the subsequent development, Wenzel and Cassie further developed their own theories in consideration of the differences in the surface conditions.
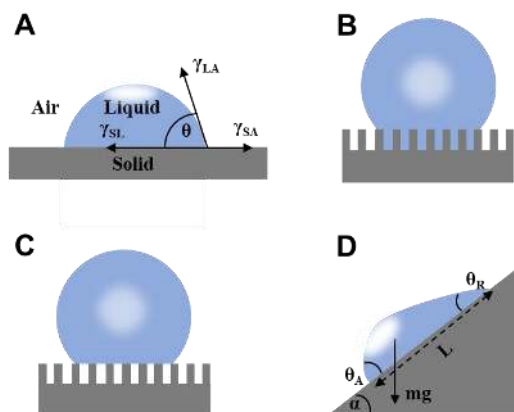


**Figure 1.** Mechanisms of liquid wetting behaviours. A) Young model, B) Wenzel model, C) Cassie-Baxter model, D) Rosano model.

**2.1.2 On a rough surface:** In 1936, Wenzel found that the rough structure of a surface enhanced the wettability of the surface due to the fact that the solid-liquid interaction area on the rough surface is larger than the apparent contact area, which can be measured by the surface roughness factor (r, which is the ratio of the actual surface area over the geometric projection area) as shown in Fig. 1B.[3, 4]

$$\cos \theta^* = r \frac{(\gamma_{SG} - \gamma_{SL})}{\gamma_{GL}} = r \cos \theta \qquad (2)$$

where $\theta^*$ and $\theta$ represent the contact angle of liquid droplet on the rough surface and the smooth surface of the same material, respectively. Under the Wenzel's contact mode, the water droplet is usually firmly adhered to the solid surface, and the apparent contact angle is increased by increasing the solid-liquid contact area.

Subsequently, Cassie and Baxter developed a new model in 1944 considering an inhomogeneous surface. Assuming that the liquid-gas contact angle was 180°, they proposed the water droplet contact angle on a rough solid surface ($\theta^*$) when air is trapped inside the surface asperity is given be the simple rule of mixture:[2]

$$\cos \theta^* = f_{SL} \cdot \cos\theta + (1 - f_{SL}) \cdot \cos 180°$$
$$= f_{SL} \cdot \cos\theta + f_{SL} - 1 \qquad (3)$$

where $f_{SL}$ represents the fractional liquid contact with the solid surface. Following Cassie's model, it is easy to see why a rough low surface energy surface display superhydrophobic contact angle (Fig. 1C). Water droplets can easily roll away on such a surface because of the much reduced solid-liquid contact area.

### 2.2 Theory of liquid sliding on tilted surface

When a droplet is not on an equilibrium state, for example, on a moving droplet on a slope, contact angle hysteresis ($\Delta\theta$) can be defined as a characteristic parameter:

$$\Delta\theta = \theta_A - \theta_R \qquad (4)$$

where $\theta_A$ and $\theta_R$ are the advancing and receding angles, respectively (Fig. 1D). Mobility of water can be measured on an inclined surface. As the tilting angle increases, the front portion of the water droplet contact angle increases due to gravity force, whereas the contact angle of the rear portion of the droplet decreases. When reaching the critical contact angle (i.e., the sliding angle $\alpha$, see Fig. 1D), the water droplet begins to slide downwards as defined by[5]

$$mg \sin \alpha = \sigma w(\cos \theta_R - \cos \theta_A) \qquad (5)$$

where m is the weight of liquid droplet, g is the gravitational acceleration, $\sigma$ is the liquid surface tension, and w the contact circle width of the liquid droplet. In the Rosano equation, the sliding angle depends on the hysteresis of the solid surface.

### 2.3 Principles of liquid transport behaviours on biological surfaces

Many plants and animals have evolved with functional surfaces demonstrating unique (non)wettability. Examples will be given next of droplets moving directionally on these surfaces, driven by the Laplace gradient, surface energy gradient, special aligned textured surfaces, and so on.

**2.3.1 Laplace gradient & Surface energy gradient:** Inspired by the spider silk (Fig. 2A) and the cactus cones (Fig. 2C),[15, 16] researchers found that the surface energy gradient and Laplace pressure play crucial roles in affecting the liquid mobility on 1-D structures. As for the special surfaces, due to the difference in surface roughness, the tension on both sides of the contact line between the water droplet and the surface is unbalanced, thus generating a driving force for water droplets to move to the direction of decreasing contact angle. This force by surface energy gradient (Fig. 2B and Fig. 2D), is given by:[17, 18]

$$F = \int_{L_j}^{L_k} \gamma(\cos\theta_A - \cos\theta_R)dl \qquad (6)$$

where $\gamma$ represents the surface tension of water, dl is the integrating variable along the length from the hydrophobic regions ($L_j$) to the hydrophilic regions ($L_k$). Hence, generated from the surface roughness difference, the surface energy gradient drives the small droplets on the spider silk and cactus spine to move from the weakly hydrophilic area (joint structure or narrow grooves) to the highly hydrophilic area (spindle-knot or wide grooves). In a word, the droplet on the spider silk and cactus spine is more realistic, which follows what the more hydrophilic area is.
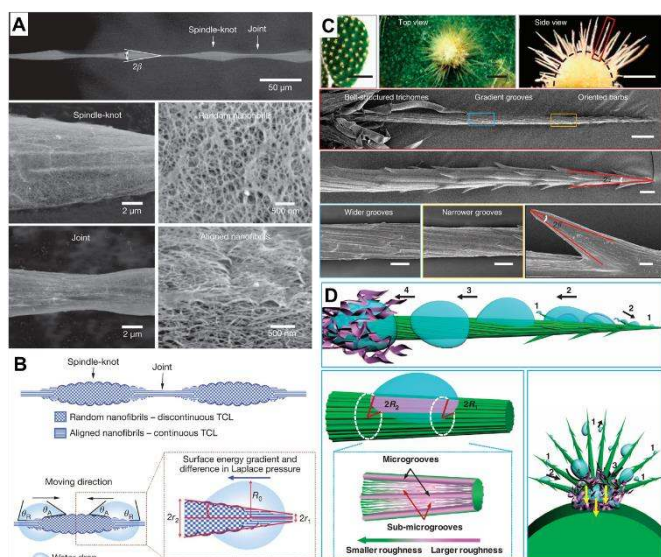


**Figure 2.** A) The SEM image of spider silk, B) The mechanism of droplet mobility on spider silk, Reproduced with permission.[15] Copyright 2010, Nature. C) The SEM image of cactus, D) The mechanism of droplet mobility on cactus, Reproduced with permission.[16] Copyright 2012, Nature.

For spider silk and conical cactus spine, Laplace gradient is the other driving force for the directional transport of water droplet, which is originated from spider silk with the spindle-shaped knots and the conical cactus spine with the aligned grooves, respectively. As for the droplet on the surface with Laplace gradient, the corresponding difference in Laplace pressure can be denoted as:[19, 20]

$$\Delta P = -\int_{r_1}^{r_2} \frac{2\gamma}{(r + R_0)^2}\sin\beta\, dz \qquad (7)$$

where $R_0$ and r are the drop radius and local radius, respectively, and $r_1$ and $r_2$ stand for the radius of the cactus spine at the tip and base sides of the droplet. The half apex-angle of the hydrophobic regions is denoted as $\beta$, and z denotes the integration variable along the diameter of the hydrophobic regions. Since $r_1 < r_2$ as shown in Fig. 2B, then $\Delta P$ (Laplace pressure difference) is greater than 0, i.e. the Laplace pressure of the joint structure is greater than the Laplace pressure of the spindle-knot section. Therefore, generated from the geometric shape difference, the Laplace pressure difference drives the water droplets to move from the thin size (joint structure or the tip of cactus spine) to the thick size (spindle-knot section or the base of cactus spine). Overall, there are two reasons for the directional water collection: the surface energy gradient and the Laplace pressure difference. The surface energy gradient force is originated from the surface roughness difference of the spider silk and cactus, and the other one is derived from the geometric shape difference of the spider silk and cactus.[15-20]

Nepenthes alata (Fig. 3A-B) enables directional continuous liquid transport on its special surface due to the hierarchical micro-nanostructured grooves (Fig. 3C-E). The asymmetric grooves with the wedge-shaped blind hole optimize and strengthen the capillary in the transport direction, and prevent backflow in the opposite direction. As discovered by Chen et al. (Fig. 3F-H), droplet can transport from the inside to the outside, while the droplet on the outer edge cannot move inside. Through observation, they found that water transport is confined within a single large channel, with large channels distributed perpendicular to the edge of the rim region, while lateral flow of water does not exceed the width of the original deposition zone. As shown in Fig. 3I, when the microcavity was filled to a water level beyond the top of its side wall, the water would wrap around the starting point of the area that overlapped the next microcavity. The lower aqueous layer (III) overflowed to produce an upper aqueous layer (II), then the upper aqueous layer filled the second microcavity; the cycle was repeated before filling the second microcavity, and the upper aqueous layer (II) overflowed to produce the top water Layer (I), the top water layer filled the third microcavity. In this way, sequential filling of each microcavity has resulted in continuous delivery of water, while retention of water prevented wetting in the opposite direction.[12]
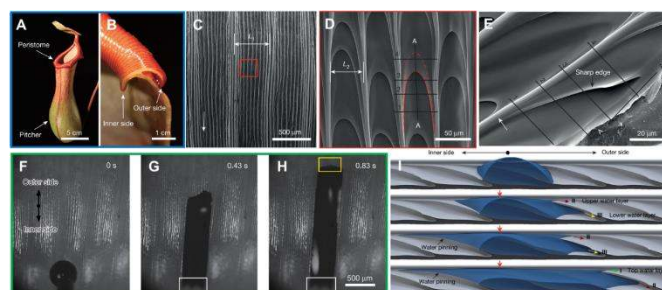


**Figure 3.** A) Optical image of the Nepenthes alata's pitcher and peristome. Scale bar: 5 cm. B) Cross-sectional optical image of the peristome from the inner side to outer side. Scale bar: 1 cm. The SEM image of C) Two first-order microgrooves and D) Approximately ten second-order microgrooves arranged on each first-order microgroove. The scale bar is 500 μm and 50 μm, respectively. E) The SEM image of duck-billed microcavity with arch-shaped edges. Scale bar: 20 μm. F-H) Water droplet transportation from the inside to the outside along a single large channel. Scale bar: 500 μm. I) 3-D simulation for the process of water droplet transportation. Reproduced with permission.[12] Copyright 2016, Nature.

**2.3.2 Liquid transport on special aligned textured surfaces:** Apart from the Laplace gradient & surface energy gradient, we can also find droplets moving directionally on aligned textured surfaces, such as butterfly, shorebirds and Namib desert beetle.

Zheng et al. found that the droplet could easily roll down from the butterfly's wings along the radial outward (RO) direction of the central axis without wetting the butterfly's body. They found that these special abilities are attributed to the numerous micro-nano scales periodically overlapped covering on the wings and the thereon fine lamella-stacking nano-stripes as shown in Fig. 4B and C. This highly directional micro-nano structure allows the water droplets to easily roll away in the radial direction but not in the opposite direction as shown in Fig. 4D and E. Especially, these two opposite states can be switched by tuning the posture of the flapping and the direction of air passing through the surface. As shown in Fig. 4F, the mechanism of the distinct adhesion is that the droplet on the butterfly's wing shows different wetting states in different inclined directions of the wing. In case of the tilted downward direction, the separation of the ordered nano-tips on the nano-stripes and micro-scales induced water droplet deposit on the wing with a Cassie-like state and form an extremely discontinuous three-phase contact line (TCL). Therefore, droplet could roll down from the surface easily. When the inclined direction was upward, the close arrangement of nano-tips and micro-scales have

pinned the droplet on the surface with a Wenzel-like state and form a quasi-continuous TCL. This anisotropic adhesion allows the butterfly wings to be directionally cleaned in a humid environment and ensures the stability of the butterfly when flying without dust accumulation.[8]
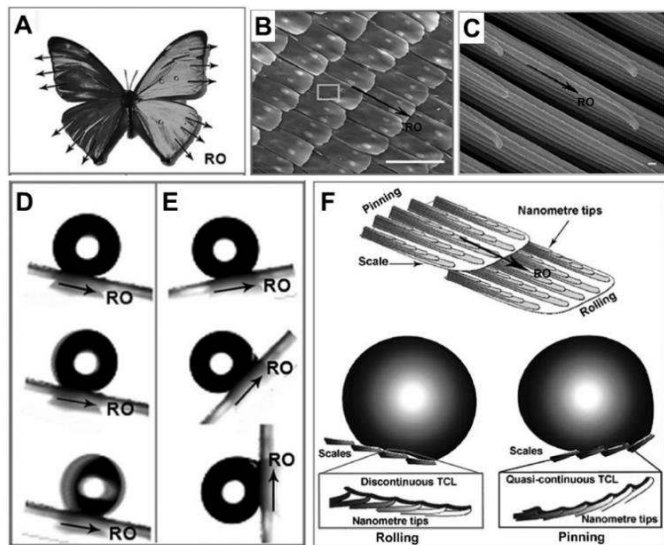


**Figure 4.** A) The optical photo of a butterfly, and the SEM images of B) the scales with micro-/nanostructures periodically overlapped covering on the wings (Scale bars: 100 μm) and C) the thereon fine lamella-stacking nano-stripes (Scale bars: 100 nm). D) The water droplet easily rolls away in the radial outward direction, but E) firmly embed in the opposite direction, even fully upright. F) The theoretical simulation for potential mechanism of these distinct adhesion. Reproduced with permission.[8] Copyright 2007, The Royal Society of Chemistry.

Withal, as for droplets transportation on shorebird's surface, Prakash et al. make a thorough research as shown in Fig. 5A. They found that the droplet could stepwise move from the tip of its beak to its mouth by bird repeatedly opening and closing its beak. As shown in Fig. 5B and C, they found that droplets advanced toward the narrower area with a constant speed firstly, then accelerated when they were close to the top of the wedge. They investigated that the drop was pinned for region $\theta_a > \theta_1 > \theta_2 > \theta_r$, marked by the red line. When $\alpha > \alpha_{break}$, the drop breaks eventually. The ratcheting regime is indicated in green and the optimal ratchet by the red arrows. For $\alpha_{open} > \alpha_{break}$, the drop breaks, whereas for $\alpha_{close} < \alpha_{close\ min}$, the drop spills from the beak as shown in Fig. 5D.[21]
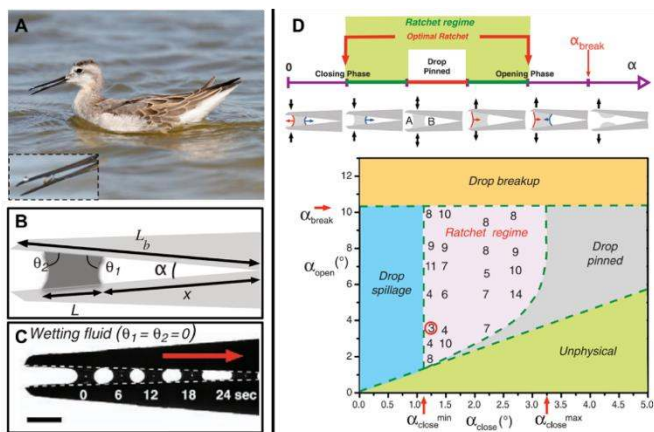


**Figure 5.** A) The photo of juvenile Wilson's phalarope feeding, the inset is fluid droplet in a horizontal beak. B) Schematic diagram of a bird beak with a fluid droplet trapped between upper and lower mandibles. C) A completely wetting droplet of silicone oil self-propels toward the apex of a mechanical bird beak with a constant opening angle. Scale bar, 2 mm. D) A schematic

illustration of droplet dynamics in an oscillating bird beak. E) Regime diagram for droplet transport in an oscillating mechanical bird beak illustrates the dependence of the system's behavior on the minimum and maximum opening angles $\alpha_{close}$ and $\alpha_{open} > \alpha_{close}$, respectively. Reproduced with permission.[21] Copyright 2008, Science.

In the Namib desert, some beetles (Fig. 6A) can survive of what? by water-harvesting dew water from air. As shown in Fig. 6B-C, Parker et al. reported that the elytra of beetles were covered in a near-random array of smooth bumps with no covering (Fig. 6B) as the hydrophilic seeding points of the peaks, where fog settled and form fast-growing droplets that pin to the elytra, starting the first process. In another aspect, due to the troughs, including their sloping sides, covering a microstructure coated in wax (Fig. 6B) with arranged regular hexagonal flattened hemispheres (Fig. 6C), the surface has created a superhydrophobic area. In the second process, water striking the hydrophobic slopes could also be collected, even though it may bounce or be blown to a hydrophilic region, when this no-collected water reaches a critical size, the ratio of water's mass to its surface contact area increased rapidly until the capillary force to the surface was overcome. Finally, the droplet is detached and roll down the tilted beetle's surface to its mouthpart, guided by other peaks along its path.[22]
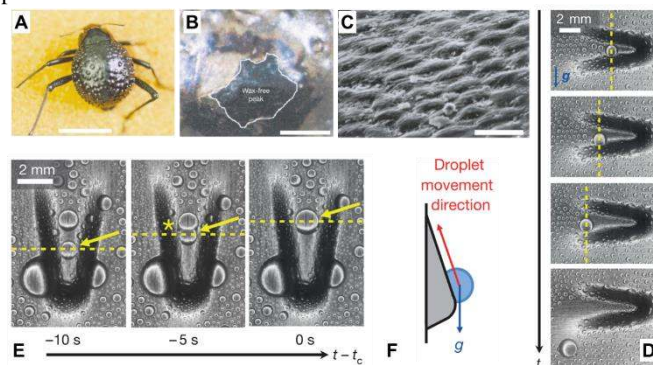


**Figure 6.** A) Dorsal optical picture of an adult desert beetle surface, covering numerous peaks and troughs. B) SEM image of depressed areas of the otherwise black elytra are stained positively (waxy, colored), whereas the peaks of the bumps remain unstained (wax-free; black). C) SEM image of the textured surface with arranged regular hexagonal flattened hemispheres. Scale bars, A) 10 mm; B) 0.2 mm; C) 10 μm. Reproduced with permission.22 Copyright 2001, Nature. D-E) Time-lapsed optical images of condensed water droplets on an asymmetric bump rotated D) 180° and E) 90° relative to gravity. F) Schematic diagram of droplet movement direction. Reproduced with permission.[23] Copyright 2016, Nature.

## 3. Liquid mobility with different orientations on super-wettability materials

As shown in Fig. 7, we divide liquid mobility into vertical motion, horizontal transportation, and interface penetration. Researchers have investigated vertical motion from two aspects: droplet self-propelling and droplet bouncing. As for the horizontal transportation, scientists have focused their researches on the driving force of motion on 1-D materials and 2-D materials. Interface penetration research includes oil-water penetration and water penetration.
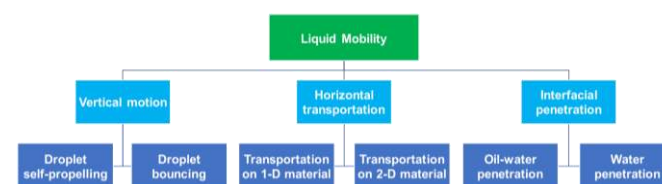


**Figure 7.** Diagram of category of liquid mobility, including vertical motion, horizontal transportation, and interface penetration.

## 3.1 Vertical motion

**3.1.1 Droplet self-propelling:** As a kind of typical solid-liquid interface dynamic motion phenomenon, condensate droplet self-propelling is an effective mode of dropwise condensation shedding, which is significant for the enhancement of heat transfer.[24] Droplet can self-propel due to the induce of surface energy released upon adjacent droplets coalesce, which experiences four stages, including condensate, growth, coalescence and jumping.[24] There are three factors, namely the surface roughness, wettability, and capability of durable superhydrophobicity, that will affect the frequency of droplet self-propelling significantly. Feng et al. verified the factors and found that nanostructures with enough narrow spacing and high perpendicularity, together with low surface energy enhance droplet self-propelling due to extremely little pinning of the condensate droplets.[25] Additionally, due to the dynamics of droplet self-propelling on materials, two significant contact mode, contact line[26] and contact line distortion[27] (shown in Fig. 8A-B), determine the dynamic droplet motion process, namely advancing, pinning, and receding modes.[26-29] Zhang et al. found that hydrophilic defect sites and hydrophobic coatings are beneficial for increasing the nucleation area and self-propelling, respectively (Fig. 8C-E).[30] When droplets condense on the surface, the self-propulsion dynamics of coalescence-induced microdroplets satisfy the equation:[30-35]

$$E_{itk} = \frac{1}{2}mV_e^2 = \Delta E_s - \Delta E_{int} - \Delta E_h - \Delta E_{vis} \qquad (8)$$

where $\Delta E_s$, $E_{int}$, $\Delta E_h$ represent the released surface energy, interfacial adhesion-induced dissipation energy, and the geopotential energy, respectively. Wang and co-workers verified that the viscous dissipation energy ($\Delta E_{vis}$) is negligible in the coalescence-induced self-propelling process unless droplets are very small (< 500 nm)[31] Tm stands for the mass of the after-coalescence droplet, and the average velocity, $V_e$ is given by:

$$V_e = \frac{1}{5}U = \frac{1}{5}\sqrt{\frac{\sigma_{lv}}{\rho R}} \qquad (9)$$

where $\sigma_{lv}$ is the liquid-vapor interface tension, $\rho$ the density of the liquid, and R the radius of coalesced droplet. $\Delta E_s$ and $\Delta E_h$ are the released surface energy and the geopotential energy respectively, and given by:

$$\Delta E_s = \sigma_{lv}\Delta A \qquad (10)$$

$$\Delta E_h = mg\Delta h = mg\left[\left(\frac{3V}{4\pi}\right)^{\frac{1}{3}} - \frac{r(3+\cos\theta)(1-\cos\theta)}{4(2+\cos\theta)}\right] \qquad (11)$$

where r is the radius of the droplet before coalescence, θ is the contact angle, ΔA and V represent the surface area difference and the volume of the coalescent droplet, respectively.
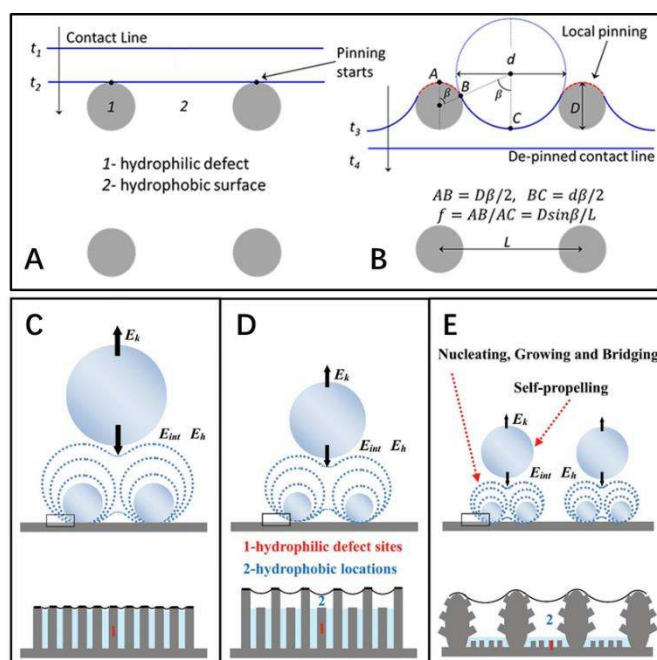


**Figure 8.** A-B) Diagram of the contact line locomotion on a hydrophobic surface "2" with hydrophilic defects "1" on the square-array substrate. Reproduced with permission.[27] Copyright 2012, American Chemical Society. C-E) Schematic diagrams of droplets self-propelling with different size and density on three types of structures with different dynamic wettability. C) nanostructure surface, D) irregular nanostructure surface, and E) hierarchical surface. Reproduced with permission.[30] Copyright 2016, Wiley-VCH Verlag GmbH & Co. KGaA, Weinheim.

Herein, based on the theoretical study of the coalescence-induced droplet movement, Nam et al. suggested that about half of the released surface energy was converted to kinetic energy in the course of coalescence.[36] Nevertheless, combining detailed measurements of droplet self-propelling with numerical modelling of droplets coalescence, Wang and co-workers believed only less than six percent of the excess surface energy can be converted to translational kinetic energy. Their research illustrated the action of internal fluid dynamics in the course of the droplet coalescence and supports the exertion of systems that can control propelling droplets.[31] Additionally, they demonstrated that the production of wetting states is caused by the conquering energy barriers as a result of nucleation-mediated droplet-droplet interactions, which provides an idea for optimizing the surface.[37]

Through regulating the roughness, coating with bionic nanofilms, and designing the nanostructured surfaces, researchers have achieved the desired functional surfaces with the ability of droplet self-propelling.[38-45] Recent literatures indicated that hierarchical superhydrophobic surfaces (SHOS) has a superior functionality of droplet self-propelling.[30, 41, 46-48] Through experiments and comparison with nanostructured surfaces, Zhang et al. demonstrated that the self-propelling movement parameters, such as the velocity and critical size of self-propelling droplet, depend on adhesive force and roughness to some extent.[48, 49] Theoretical experiment results demonstrate that hierarchical SHOS has the most superior condensate microdroplet self-propelling (CMDSP) functionality due to the lowest adhesion and highest roughness.[34]

To effectively obtain dropwise condensation and enhance the ability of droplet self-propelling, condensate must be quickly removed from the surface, which contributes to enhance heat transfer coefficient of materials.

**3.1.2 Droplet bouncing:** Droplet bouncing on nonwetting surfaces experiences two stages, namely a spreading out stage (to a maximum diameter), followed by a recoil stage (to an original state) before rebounding off the substrate.[50] Amongst all the factors on drop bouncing performance, surface roughness, wettability, substrate temperature, environmental conditions and air-cushion have significant effect.[51-58]

Three dimensionless parameters are often used in the fundamental research on droplet bouncing.[59] The first is the Weber number (We), which is the ratio of the inertial force to the surface tension. When the Weber number is smaller than 1.0, it means the surface tension plays a significant role. When the Weber number surpasses 1.0, it means the effect of surface tension is negligible. The second parameter is the Reynolds number (Re), which is the ratio of the inertia force to the viscosity force. When the Reynolds number is small, it indicates the viscosity influence is higher, and vice versa. The third parameter is the Ohnesorge number (Oh), which is approximately the ratio of viscous forces to the product of inertial and surface tension forces. Related formulae are shown below.

$$We = \frac{\rho v^2 D_0}{\gamma} \qquad (12)$$

$$Re = \frac{\rho v D_0}{\mu} \qquad (13)$$

$$Oh = \frac{\mu}{\sqrt{D_0 \sigma \rho}} \qquad (14)$$

where $\rho$, $D_0$, and $v$ represent the liquid drop density, diameter, and impact velocity, respectively. Surface tension and dynamic viscosity are represented by $\gamma$ and $\mu$, respectively.

The velocity and viscosity play indispensable roles in deciding the wetting states of an impinging droplet to be either completely pinned, partially or entirely bounced, or even splashed.[60-62] For the droplet with a low We, the impact is quasi elastic with a minor-scale deformation due to the insignificant energy dissipation. For large We and Re, the droplet tends to splash into two or more secondary disintegrated droplets.[51, 53, 59, 61] Based on the dimensionless parameters,[60, 62-68] Quéré et al. found that the kinetic energy of the impacting droplets is dissipated by viscosity in the course of impact in the viscous-inertial system,[64] the maximum diameter obeys $D_{max} \sim D_0 Re^{1/5}$.[69, 70] As for a viscous droplet, Schroll et al. simulated the impact of a viscous liquid droplet onto a smooth dry substrate. Since the ambient air pressure is negligible, droplets with several m·s$^{-1}$ impacting speed would not produce a splash. Due to the action of the boundary layer produced by droplet impacting, the falling droplet would be flattened into a spatially uniform thin pancake shape.[67] Therein, the pancake ejection is subject to the impacting speed and liquid viscosity.[66] As for the capillary-inertial system, the kinetic energy of the impacting droplet could be entirely converted into surface energy,[14] the maximum diameter obeys $D_{max} \sim D_0 We^{1/2}$ or $We^{1/4}$.[64] Recently, Visser et al. have observed that no splashing happened for droplet diameters between 12 and 100 µm with impacting speed up to 100 m s$^{-1}$. Compared with previous available models, the experimental result corresponds with the Pasandideh-Fard model,[71] in which the boundary layer dynamics has a significant impact on the droplet spreading. Utilizing the model input value with an initial contact angle of 180°, they confirmed that the air layer was present underneath the impinging droplet, which was further verified by de Ruiter et al., who presented a universal bouncing mechanism that the air film could occur continuously on both wetting and nonwetting surfaces for the droplet with moderate impacting speed.[65]

The contact time, defined as the time from the beginning of the droplet impacting on the substrates to the ending of bouncing off the surfaces, can be used to characterize the droplet dynamic. In 2002, Quéré et al. measured the contact duration between a droplet and the substrate, then quantified the performance of superhydrophobic surfaces.[14] As for a droplet impacting on superhydrophobic surfaces, its inertial-capillary nature can be considered, but its viscosity effect are not important and can be ignored. Balancing inertia ($\rho R/\tau^2$) with capillarity ($\gamma/R^2$), the contact duration obeys:[14, 72]

$$\tau \approx \sqrt{\frac{\rho R^3}{\gamma}} \qquad (15)$$

The contact time is linearly correlated with $R^{3/2}$ in the range of droplet radius from 0.1 mm to 4.0 mm, and has no correlation with the impacting speed from 20 cm s$^{-1}$ to 230 cm s$^{-1}$ but increases in this range below 10 cm s$^{-1}$ because of the drop's weight (Fig. 9A).[14, 72]

Noteworthily, compared with the contact duration of the inertia-dominant spreading stage, the duration of recoiling stage accounts for a large proportion with about 70-80% of the total contact duration. Bartolo et al. divided the recoiling stage into two regimes: viscous regime and inertial regime. Herein, the droplet recoiling rate ($V_{ret}$ /$D_{max}$) depends on viscous force and surface tension forces.[73] As for the inertial regime, the recoiling rate obeys Equation (16) according to the Taylor-Culick approach[74, 75], where $\tau_i$ and $\theta_r$ represents the inertial time and the receding contact angle, respectively; As for the viscous regime, the retraction rate obeys Equation (17):[53, 73]

$$\frac{V_{ret}}{R_{max}} \sim \frac{\sqrt{1 - \cos\theta_r}}{\tau_i} \qquad (16)$$

$$\frac{V_{ret}}{R_{max}} \sim \frac{\mu R_0}{\gamma} \qquad (17)$$

Researchers have demonstrated that the time during impacting and bouncing depends on wetting hysteresis and the solid fraction.[76, 77] Using superhydrophobic surfaces, Bird et al. have managed to reduce the contact time below the theoretical limit. This is due to the redistribution of the liquid mass and thereby altering the drop hydrodynamics.[50] Similarly, Quéré and co-workers have significantly changed the hydrodynamics by creating a macrotexture to maximize the water repellence and minimize the contact time between solid and liquid even further.[78] Shen et al. observed that the impacting droplet was disintegrated into several smaller portions in the presence of the "cross-shaped" macrotextures, and the recoiling process could be completely integrated into the spreading process to the maximal deformation, resulting in a much shorter overall contact duration of approximately 5.5 ms (Fig. 9B).[77] Meanwhile, Wang and co-workers found that pancake bouncing on the surface experienced a deep penetration and detachment, but did not experience the process of retraction. This allows a fourfold reduction in contact time on superhydrophobic surfaces, due to the rectification of capillary energy stored in the penetrated liquid into upward motion adequate to lift the drop.[79] Soon after, they discovered that a droplet impacting on Echevaria leaves displays asymmetric bouncing dynamics with different spreading and retraction along two directions, and they attribute this phenomenon to the concave/convex architecture of cylindrical leaves. Furthermore, they concluded that the contact time could have a ~40% reduction, towing to the asymmetric momentum and mass distribution caused by the preferential fluid pumping around the drop rim.[80]
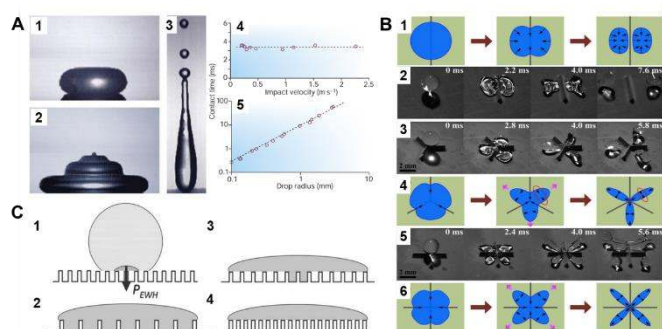
**Figure 9.** A) Mechanism of droplet impacting and bouncing on the substrate surface. 1-3, the process of droplet impacting, recoiling and bouncing, respectively. 4-5, The function diagram of impacting droplet contact time with impacting speed and droplet radius. Reproduced with permission.[14] Copyright 2002, Nature Publishing Group. B) Droplet impacting processes on superhydrophobic surfaces with different macrotextures. Reproduced with permission.[77] Copyright 2015, AIP Publishing LLC. C) The wetting states of impacting droplets based on different relative magnitude of the wetting and antiwetting pressures. Reproduced with permission.[81] Copyright 2009, American Institute of Physics.

Irreversible wetting state transition between Cassie state and Wenzel state will cause the absence of the anti-adhesive phenomenon corresponded with superhydrophobicity.[81-91] Presently, the mechanism about wetting state transition is still under discussion. Inspired by the research of Lafuma and Quéré,[88] researchers focused on the smart structure design to avoid the irreversible wetting state transition.[83] Through utilizing a superhydrophobic rough specimen with a two-level hierarchical structure, Quéré et al. achieved Cassie regime stabilization and water repellency enhancement. Additionally, they verified the optimal conditions for the structure design to achieve droplet bouncing without satellite ejection and confirmed that the critical value of We number for the satellite ejection is about 160, which is lower than that of a hydrophobic flat surface (We number of about 700) and hydrophilic surface (We number > 1000). Additionally, they emphasized the significance of the air film in minimizing the viscous dissipation, and demonstrated the conditions of pinning would occur when the velocity obeys:[89]

$$V > V^* = \sqrt{\frac{\gamma h}{\rho l^2}} \qquad (18)$$

where h is the micropillar's height, l the adjacent micropillars' distance, and $V^*$ the critical speed. Afterwards, Bartolo et al. verified that the dynamic pressure ($P_D$) was a crucial factor. Once it exceeds the capillary pressure ($P_C$), the Cassie-Wenzel wetting state transition inevitably occurs. $P_D$ and $P_C$ are given by:[82]

$$P_D = \frac{1}{2}\rho V_1^2 \qquad (19)$$

$$P_C = \frac{\sigma}{a}\left[\frac{-4\cos\theta_a}{\left(1+\frac{b}{a}\right)^2 - 1}\right] \qquad (20)$$

where $\theta_a$ represents the advancing angle on the smooth surface, a and b are the pillar width and the distance between pillars, respectively. Three regimes were identified, that is the fakir regime (for droplet with small impacting speed), bouncing regime (for droplet with moderate impacting speed), and sticky regime (for droplet with high impacting speed). Using the lattice Boltzmann method, Hyväluoma and Timonen verified Bartolo et al.'s investigation and presented another possible regime, the non-bouncing fakir state for droplet with

the impacting speed lager than that of bouncing droplet but smaller than that of sticky droplet.[85] However, when compared to the investigation by Bartolo et al., their calculated antiwetting capillary pressure ($P_C$) was considered to have far exceeded the theoretical value of dynamic pressure ($P_D$) calculated by Equations (19) and (20).[87] The water hammer pressure ($P_{WH}$) was also employed to predict the transition into the Wenzel state.[81, 84, 87] and defined as:

$$P_{WH} = k\rho VC \qquad (21)$$

where *k* is a constant depending on the nature of impacting surface and the droplet impacting speed, C and V stand for the sound velocity and the terminal droplet speed, respectively. Deng et al. used the water hammer pressure ($P_{WH}$) to define three wetting states of the impacting droplet clearly, viz: total wetting state ($P_{WH} > P_D > P_C$), partial wetting state ($P_{WH} > P_C > P_D$), and total nonwetting state ($P_C > P_{WH} > P_D$), as shown in Fig. 9C.[81] In general, the Cassie-Wenzel regime transition relies on the interaction of impacting speed, geometric parameter, materials nature, and liquid properties.[84, 86, 91] Remarkably, when a droplet bounces off the substrate surface, how to regulate the direction is significant to the droplets motion track.[92-96] Utilizing the modified substrates with variable density textures, Quéré and his co-workers found that the impacting droplets bounce off obliquely. They have systematically presented a bouncing direction transition mechanism, and verified that asymmetry or anisotropy would induce the liquid motion toward the zone with the high texture density.[95] By fabricating nonuniform textures to achieve roughness gradients surface, Wang and co-workers verified that the gradient surface can achieve the droplet rebound axially following a specified lateral trajectory imparted by the wetting gradient.[94] In addition, they found that whether the self-migration trajectory is towards or against the wettability gradient, it depended on the competition between the capillary pressure and water hammer pressure. This finding is different from the previous reports that the self-migration trajectory is towards the wettability gradient,[96] but could be significant for the future research progress and applications.

From the above review, it is clear that the roughness and wetting transition significantly affect the bouncing performance, including direction alteration, and contact time reduction. Let us not to forget that the substrate temperature also affects the bouncing performance. As observed by Leidenfrost, when the water droplets are placed on a hot substrate, droplets will bounce and roll around on the substrate before they are evaporated. The air cushion between the underlying substrate and imping droplets is a key factor behind the observation,[13] and the air cushion can be stabilized through the control of phase change process. When the substrate temperature T is above the liquid's boiling point, the droplet may experience three different regimes as shown in Fig. 10A-C, depending on the competition between the Leidenfrost temperature and substrate temperature. The three regimes are contact boiling (contact the surfaces and boil immediately), gentle film boiling (form a Leidenfrost vapor layer without any surface contact and bounce back), and spraying film boiling (both form the Leidenfrost layer and eject tiny droplets upward). Tuan et al. experimentally determined the conditions under which impact behaviours in each regime can be realized as shown in Fig. 10D.[56]

So far, researchers have successfully fabricated various substrates covered with micro-structure,[100-102] nano-structure,[103-105] and micro- & nano-structure,[106-109] to intensify heat transfer via enhancing the Leidenfrost temperature. Utilizing surfaces covered with carbon-nanofibers, Hrudya et al. found that it has delayed the transition to film boiling to much higher temperatures compared to smooth surfaces. The vapor flow cools the small scale of the carbon fibers before the liquid impact, thus enhances the Leidenfrost

temperature.[103] It was also found that the size of the micro-structure or micro- & nano-structure has a significant effect on the Leidenfrost temperature.[101, 102]
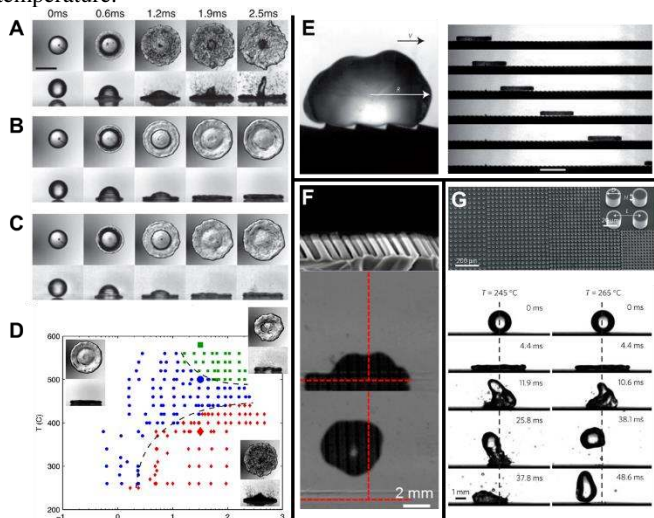


**Figure 10.** Series of bottom-view and side-view images of representative water droplet impacts in three regimes. A) Contact boiling, B) Gentle film boiling, C) Spraying film boiling. D) Phase diagram for water droplet impact on a heated surface showing three separate regions: contact boiling regime (red solid diamonds), gentle film boiling regime (blue solid circles), spraying film boiling regime (green solid squares). Reproduced with permission.[56] Copyright 2012, American Physical Society. E) A drop deposited on a hot ratchet and self-propels in the direction indicated by the arrow. Reproduced with permission.[97] Copyright 2011, Nature. F) Cross-sectional SEM image of tilted nanopillar arrays and the corresponding images of water droplet impact and subsequent rebound. Reproduced with permission.[98] Copyright 2013 American Chemical Society. G) Scanning electron microscopy (SEM) image of the gradient surface and the corresponding of the vectored propulsion of an impinging droplet for temperatures T=245 °C and 265 °C, respectively. Reproduced with permission.[99] Copyright 2016, Macmillan Publishers Limited.

Utilizing Leidenfrost droplet, researchers have developed various substrates to investigate directional droplet transport. Quéré's group found remarkably mobile model hovercrafts, the droplet placed on a hot ratchet not only levitates, but also self-propels in a well-defined direction as shown in Fig. 10E. This is attributed to the asymmetric textures rectification effect on vapor flow escaping below the Leidenfrost body.[97]

As for these macro- and microscale ratchet structures, the vapor flow is dominant and the Leidenfrost droplet moves against the tilted direction,[110-115] whereas for the surfaces with tiny features, droplets move along the tilted direction as shown in Fig. 10F.[98, 116, 117] Asymmetric wettability of nanostructured surfaces was found to have induced the observed directional rebound of droplets in the transition boiling regime.[98] Liu et al. found that tilting silicon nanowires surfaces can be utilized to transport a drop directionally at high temperature through regulating its surface characteristics. Superhydrophilic surfaces covered with tilting silicon nanowires with moderate-lengths were found to display anisotropic wetting performance at high temperature. Surfaces with enhanced chemical hydrophobicity or covered with short tilting silicon nanowires showed high-temperature non-wetting performance, and thus failed in driving the drop transport directionally. Superhydrophilic surfaces with long tilting silicon nanowires caused the deposited drops to boil violently and were not suitable for directional drop transport at high temperature.[117]

It is challenging to control and induce the motion of the highly mobile droplets towards specific locations without affecting the heat transfer efficiency. Wang's group reported that the wetting symmetry

of a droplet could be altered at high temperature by generating two concurrent thermal states (Leidenfrost and contact-boiling) on a topographically patterned surface, thus leading to a preferential motion of a droplet towards the region with a higher heat transfer coefficient as shown in Fig. 10G. This is beneficial for some applications, such as tuneable control of directional fluid flow, varying heat transfer, and modification of the critical Leidenfrost temperature.[99]

## 3.2 Horizontal transportation

**3.2.1 Transportation on 1-D materials:** Zheng's group fabricated various artificial spider silk and investigated the motion of water droplets. They found that water droplets tend to move to the wetter area with higher surface energy. As shown in Fig. 11A, when randomly condensed microdrops grew increasingly on the joint and spindle-knot, a coalesced droplet formed and tended to move away or toward to the knot as shown in Fig. 11B. This is ascribed to the unbalanced forces acting on the two ends of the droplet contact lines. Additionally, they predicted a critical size of ≈15.5 μm through a linear fitting the test data as shown in Fig. 11C-D.[118] Subsequently, they verified that the hump structures of spindle knots on the fiber have contributed to the motion of condensed water droplets,[119-121] and regulating the period and the scale of spindle knots can further improve and enhance the mobility of water droplets.[122-124] To further improve the mobility of water droplets and realize its transportation over a long range, they fabricated fibers with gradient structure by a tilted dip-coating method (Fig. 11E). Attributed to the multistage synergy of the released energy from microdroplets coalescence (Fig. 11F), the capillary adhesion force, and Laplace pressure gradient along the gradient structure, water droplets can directionally move quickly over a long distance,[125] as illustrated in Fig. 11G. The tiny water condensed drops first start directional transport and move toward spindle-knot, then they coalesce with the neighbour drops. Subsequently, the coalesced droplet transports towards a bigger spindle-knot to stay at a stable state through the synergy of Laplace pressure (ΔP) gradient and released energy from droplets coalescence ($F_{cr}$). The Laplace pressure gradient (ΔP) can be described in the previous Equation (7). Finally, the coalesced droplet slides from the joint of bigger spindle-knot towards the biggest one due to $F_{ca}$ (small spindle-knot) < $F_{ca}$ (big spindle-knot), which reduces the angle ($\alpha_1$) between liquid surface and spindle-knot. According to Wenzel's law,[4] the capillary force ($F_{ca}$) which is induced by the roughness can be described as:

$$F_{ca} = r \cdot 4\pi b\gamma \sin(\pi - \alpha) \qquad (22)$$

where r is the roughness, b is the silk effective radius ($b_{small\ knot} < b_{big\ knot}$), α is the angle between liquid surface and spindle-knot.
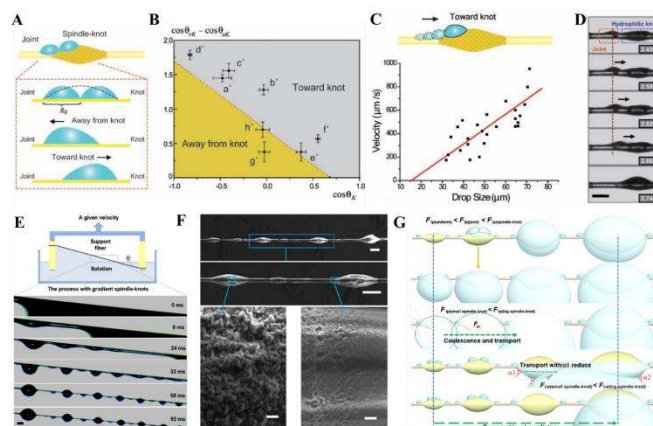
**Figure 11.** A) Analysis diagram of forces that can drive tiny water droplets away from and toward knot. B) The functional relationship between static contact angle ($\cos\theta_K$) on the spindle-knots and the difference which is between receding and advancing contact angles ($\cos\theta_{rK} - \cos\theta_{aK}$). C) Functional relationship diagram between the velocity toward knot and the drop size on the fiber with the rough spindle-knot. Reproduced with permission.[118] D) The motion of tiny water droplets on the fiber with the rough spindle-knot. Copyright 2010, WILEY-VCH Verlag GmbH & Co. KGaA, Weinheim. E) Schematic diagram of the whole fabrication process. F) SEM images of bioinspired fibers with gradient spindle-knots with various scales. G) Mechanism illustration of the water droplets transportation in a long distance. Reproduced with permission.[125] Copyright 2013, Nature.

**3.2.2 Transportation on 2-D materials:** 3.2.2.1 Unidirectional line-pattern surface: The movements of liquids resulting from unbalanced surface tension forces constitute an important surface phenomenon, known as the Marangoni effect.[126] When regulated properly, these types of flows are valuable in several industrial applications. Apart from the variations in temperature or composition on a liquid surface, the surface tension heterogeneity on a solid substrate can also induce the usual Marangoni motions. Due to the surface tension gradient, the motion of droplets can be directional and controllable.

Bliznyuk et al. created anisotropic patterns with stripes of alternating wettability (Fig. 12A) through lithograph to investigate the motion of droplets. By altering the relative widths of the stripes, the fraction of the hydrophobic area was varied to ensure the energy gradient that could induce the motion of the droplets as shown in Fig. 12B. The fraction of the hydrophobic area α can be described as:

$$\alpha = \frac{w_{pho}}{w_{phi}} \qquad (23)$$

where $w_{pho}$, $w_{phi}$ stand for the width of superhydrophobic and superhydrophilic area, respectively. They found the velocities of liquid spread were higher than the non-structured surface energy gradients, which is attributed to the anisotropic patterns that created a privileged direction for liquid spreading along the parallel stripes and confined the motion along the perpendicular stripes (Fig. 12C-D).[127] Furthermore, based on the previous research, Wu et al. fabricated three prepared unidirectional stripes with gradient wettability patterns to study the dynamic behavior of droplets on these unidirectional channels as shown in Fig. 12E. Three prepared unidirectional stripes were designed with distinct wettability-patterned gradients (Δ = 1, 1.5 and 2) to control the displacement of droplet movement (Fig. 12F). The wettability-patterned gradients can be described as:

$$\Delta = \frac{\Delta P}{w_0} \qquad (24)$$

where $w_0$ is the width of superhydrophobic stripes units, P is the width between two adjacent stripes, ΔP stands for the spacing increment of P. By regulating the density and placement of gradient wettability patterns, they succeeded to regulate the movement displacements of droplets (Fig. 12G-J). Research indicates that increasing the wettability-patterned gradients favors the movement displacements of droplets, which can be applied in self-driving rapid fluid transportation.[128] Additionally, Ghosh developed a wedge-patterned surface through laser printer-based photo-masking and showed controlled liquid transportation at large flow rates on flat and tilted patterned surfaces($\sim$350 μL s$^{-1}$). The surface tension from wedge pattern restricted tracks on the on-limits units and drove the liquid to move from the narrow superhydrophilic wedge side to the wide side without any energy input, even when resisting against gravity. The driving capillary force linearly increases with the wedge track angle, but the displacement decreased with the angle. Therefore, how to

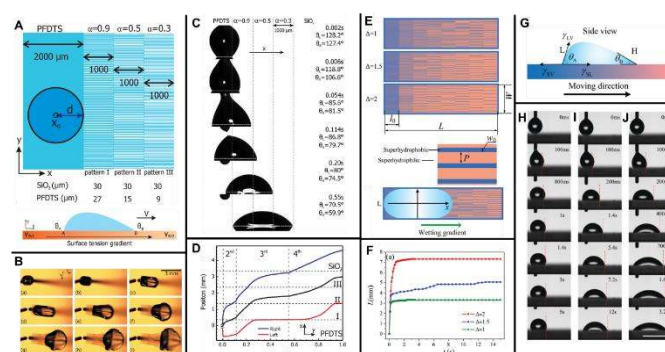balance the transport velocity and displacement will be a key point in the future.[129]



**Figure 12.** A) Schematic diagram of the gradient pattern design and Surface tension gradient on a silicon slice. Hydrophobic (blue) and hydrophilic areas (white) are PFDTS SAMs and bare SiO$_2$, respectively. B) The movement of glycerol/water droplet with a volume of 2 μL on a surface with subsequent pattern gradient α = 0.9, 0.5, 0.3. C) The side view picture of droplet displacement snap shots on the corresponding pattern gradient surface (d = 0.36 mm). D) The displacement variation of the left (receding) and right (advancing) boundaries over time; the center position stands for the average of both boundaries. Reproduced with permission.[127] Copyright 2011, American Chemical Society. E) Three designed samples of unidirectional stripes on a photomask. Blue and orange stripes stand for superhydrophobic and superhydrophilic areas, respectively. F) The displacement variation over time on three surfaces with different wettability-patterned gradients. G) Side view diagram for a droplet standing on a wettability-patterned gradient surface. H-J) Snap shots of the water droplet movement on three unidirectional stripe-patterned gradient surfaces, respectively. The scale bars for all figures are 5 mm. Reproduced with permission.[128] Copyright 2017, The Royal Society of Chemistry.

3.2.2.2 Radial inward- & outward-pattern surface: Apart from the unidirectional wettability-patterned gradients, radial wettability is also reported for some specific applications, such as water-harvesting. Different from the two-dimensional random motion of merging droplets, Daniel et al. designed a radially outward chemical gradient through diffusion-controlled silanization method to guide the otherwise random motion of droplets as shown in Fig. 13A-D. Due to the hysteresis, the driving force of the droplet movement could be gained from the difference of the equilibrium contact angles at points at B and A as shown in Fig. 13E. Additional driving force is provided by the coalescence with the adjacent droplets that nucleate and grow prior to the primary droplet formation. Powered by these driving forces, water droplets (0.1 to 0.3 mm) can transport with a velocity hundred to thousands of times faster than that of typical Marangoni flows. The enhancement of the heat transfer coefficient on the surface with a chemical gradient, as shown in Fig. 13F, could be applied to the heat exchangers and heat pipes.[18] Similarly, Hong developed a controlled oxidation reaction to fabricate radially inward wettability gradient surfaces with hydrophilic centers and hydrophobic exteriors, which is a little different from Daniel's radially outward gradient surfaces.[18] Due to the coalescence of dewdrops and the wettability gradient, water droplets moved toward the hydrophilic center and went through the collected hole, which can be applied for water-harvesting.[130]
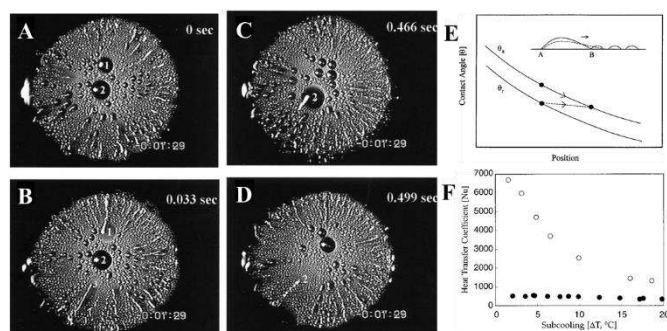
**Figure 13.** A-D) Snap shots of fast water droplets movements (displayed by the plume-like and streak-like patterns) on a silicon slice with a radial wettability gradient. E) The contact angles ($\theta_a$: advancing contact angle; $\theta_r$: receding contact angle) variation as a function of time. F) The diagram of heat transfer coefficient for the siliconized copper surface (solid circle) and the chemical gradient copper surface (hollow circle) as a function of subcooling. Reproduced with permission.[18] Copyright 2001, Science.

Furthermore, different from the circle pattern with inward or outward wettability gradients, Bai et al. successfully prepared surfaces with various shaped wettability patterns to compare the fog-harvesting performance as shown in Fig. 14A. They found that surfaces with star-shaped pattern possessed more efficient fog harvesting than other uniform surfaces, viz. superhydrophilic, superhydrophobic, and circle pattern (Fig. 14B-E). Additionally, surfaces with a smaller pattern size were found to be more efficient than the ones with a larger pattern size of the same pattern. The finding means that both the shape and size of the pattern are crucial for the liquid directional transport and thus the water collection efficiency.[131]
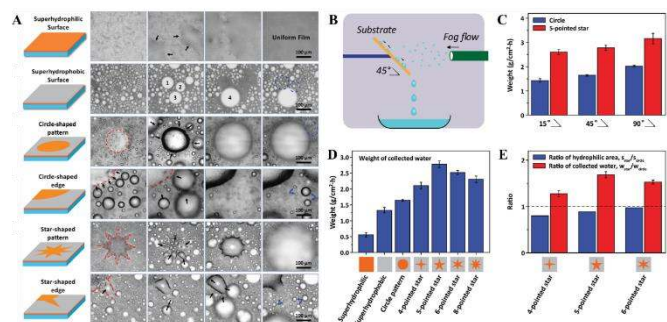


**Figure 14.** A) Snap shots of the fog-harvesting process on surfaces with different wettability pattern. B) Schematic illustration of the strategy to measure the fog harvesting performance on different surfaces. C) Comparison diagram of fog harvesting efficiency on circle and 5-pointed star patterns with different tilting angle. D) Comparison diagram of fog harvesting efficiency on surfaces with various wettabilities. E) Ratios of hydrophilic area and collected water on 4-, 5-, 6-pointed star patterned surfaces, respectively. Reproduced with permission.[131] Copyright 2014, Wiley-VCH Verlag GmbH & Co. KGaA, Weinheim.

3.2.2.3 Directional transportation on bio-inspired Nepenthes alata surface: The pitcher plant is known for its subtle pitcher cage that can easily capture insects due to this well-designed trap with a slippery peristome. Inspired from that, scientists gradually focus their eyes on the biomimetic artificial peristome surface of pitcher plant with water-collecting functionality. Recently, exploiting two typical lithography strategies, Jiang's group fabricated novel microgrooves with a concave array at their bottom. Through the test of the concave outline's effect on asymmetrical liquid spreading, they found that the arch-shaped outline and sharp rim on the concave edge were crucial for the directional liquid spreading.[132] Thereafter, they proposed and demonstrated spontaneous overflow-controlled liquid unidirectional transportation mechanism using the peristome-mimicking surface. Liquids with varied surface tensions and viscosities can spontaneously

propagate in a single preferred direction and pin in all others, which is different from the canonical predictions for completely wetting liquids spreading symmetrically on a high-energy surface.[133] These functionalities of fast, long-distance and unidirectional transportation on the biomimetic surface could be applied in many fields like fog-harvesting, nonpowered drug delivery, and self-lubrication.

### 3.3 Interface penetration

Apart from the vertical motion and horizontal transportation, interface penetration is another form of liquid mobility. As a mode of motion from front side to back side along the vertical direction, interface penetration can be applied for oil-water separation. Recently, directional liquid penetration through the porous materials has been investigated by several research groups, as illustrated below.

**3.3.1 Oil-water penetration:** The mechanism of oil-water penetration in porous membranes depends on the types of materials used, which may display superhydrophobicity-superoleophilicity, superhydrophilicity-superoleophobicity, superhydrophilicity-underwater superoleophobicity, and stimuli-responsive wettability.

3.3.1.1 Superhydrophobic-superoleophilic wettability: Membrane surface that has superhydrophobic-superoleophilic wettability is used for oil-water separation, where oil or water can selectively wet and pass through the membrane.[134-148]

Tian et al. reported a stable superhydrophobic and superoleophilic coating based on a stainless steel mesh with aligned ZnO nanorod array-coated mesh film (Fig. 15A). As shown in Fig. 15B, the treated mesh film displays both superhydrophobic (Fig. 15B1) and superoleophilic (Fig. 15B2) properties, which can make oil spread on the coated membrane quickly over and breakthrough easily. When a certain kind of liquid stands on the film surface, its meniscus is stable. Attributed to the surface curvature, its intrinsic contact angle $\theta$ can be sustained wherever the position of three-phase contact line is (as shown in Fig. 15C). Once external pressure works, the liquid like water cannot penetrate the film spontaneously when $\theta > 90°$ due to the static pressure $\Delta P > 0$. Whereas when $\theta < 90°$ due to the static pressure $\Delta P < 0$, the mesh film cannot sustain any pressure, the liquid like oil can penetrate the film spontaneously. As for the surface with aligned ZnO nanorod arrays, the structured film can increase the advancing contact angle of water droplet, and decrease that of oil droplet on the surface, which makes the penetration more efficient. Through comparison as shown in Fig. 15D, they found the pore size plays a significant role in the level of hydrophobicity. Among them, the surface of aligned ZnO nanorod arrays with pore size of 50 μm was found to be optimal for the desirable superhydrophobicity.[145]

Membranes that have asymmetric wettability can be an excellent material for liquid penetration. Hu et al. constructed bilayer membranes made of a polydopamine-coated single-walled carbon nanotube layer (SWCNTs) and a covered SWCNT layer. When $P_{oil}$ (the intrusion pressure of oil) < $P_{applied}$ (the applied pressure difference across the membrane) < $P_{water}$ (the intrusion pressure of water), the hydrophobic-superoleophilic surface can efficiently separate surfactant-stabilized water-in-oil emulsion. As for a higher $P_{applied}$ ($P_{water}$ < $P_{applied}$ < $P_{asy}$), the cooperative effect of dual layers can achieve the capability of separating surfactant-stabilized oil-in-water emulsion (Fig. 15E). As shown in Fig. 15F-G, such ultrathin bilayer membranes display ultrahigh penetration flux and separation efficiency with excellent antifouling for controlled single-system oil-water emulsion separation by simply adjusting $P_{applied}$.[135]
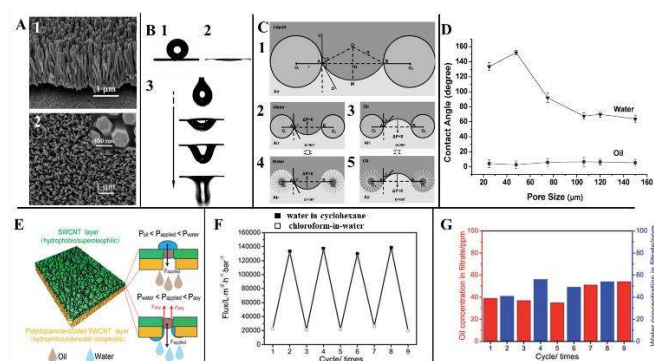
**Figure 15.** A) The view of the aligned ZnO nanorod array-coated stainless steel mesh film, 1) the side view, 2) the top view. B) Special surface wettability, 1) water droplet, 2) liquid paraffin oil, 3) the dynamic process of an oil droplet penetrating through the mesh film. C) Theoretical model of the liquid wetting on the surface with aligned ZnO nanorod arrays. D) The water and oil contact angles on the surface with aligned ZnO nanorod arrays as a function of the pore size. Reproduced with permission.[142] Copyright 2011, the Owner Societies. E) The schematic structure of an ultrathin bilayer membrane, and the corresponding pressure response mechanism diagram for oil-water separation. F) The switchable penetration flux keeps stable after several cycles. G) water (blue bar) and oil (red bar) concentration in the filtrate. Reproduced with permission.[135] Copyright 2015, The Royal Society of Chemistry.

3.3.1.2 Superhydrophilic-superoleophobic & superhydrophilic-underwater superoleophobic wettability. Inspired by the shark skin with the self-cleaning functionality enabled by underwater superoleophobicity, researchers focus more attention on the other typical mechanism of oil-water separation, viz. superhydrophilic-superolephobic and superhydrophilic-underwater superoleophobic wettability.[149-163]

By depositing titanium oxide nanoparticles onto fabric, Zheng et al. fabricated micro- and nanoscale hierarchical-structured superhydrophilic fabric films with under-water superoleophobicity. As shown in Fig. 16A-D, Due to the superhydrophilicity of the scaly nanostructured titanium oxide film, water can spread and wet the fabric film without air bubbles on the membrane surface. When oil-water mixture was poured onto the fabric film (Fig. 16E-G), the scaly fabric film could absorb water to achieve saturation rapidly in all regions of the contact before the oil could wet the film. Therefore, the water penetrates the film rapidly, while the oil is left on the film due to the excellent superoleophobicity in water. This experiment verifies the scaly titanium-oxide-coated fabric films possess the functionality of the effective oil-water separation. Whereas as for the original fabric, the oil can gradually wet the fabric with some air bubbles and penetrate through these regions attributed to the superoleophilicity of the fabric in air. Therefore, the original fabric without the coating does not possess the ability of effective oil-water separation.[163]

However, traditional single membrane devices with oil-water separation functionality have inherent limitations when dealing with different kinds of oil in water. Liu et al. designed an integrated oil-water separation system, consisting of superhydrophobic oxidized copper mesh with an anti-water (AW) function and polyacrylamide (PAM) hydrogel coated superhydrophilic copper mesh with an anti-oil (AO) function as shown in Fig. 18H. They integrated two membranes into a two-outlet pipe equipment (Fig. 18I) and investigated the efficiency of different kinds of oil-water separation. When the oil density is smaller than that of water ($\rho_{oil} < \rho_{water}$), the configuration of AO membrane and AW membrane is placed on the lower and higher outlet, respectively, will benefit heavier water to sink and penetrate through the below AO membrane, meanwhile lighter oil to float and penetrate through the upper AW membrane. If the oil is heavier than water ($\rho_{oil} > \rho_{water}$), the placement of the two membranes

can be simply swapped. Compared with traditional single membrane devices with oil-water separation functionality, such a functionally integrated system achieves continuous synchronized separation of oil and water, which significantly increased the separation efficiency.[164]
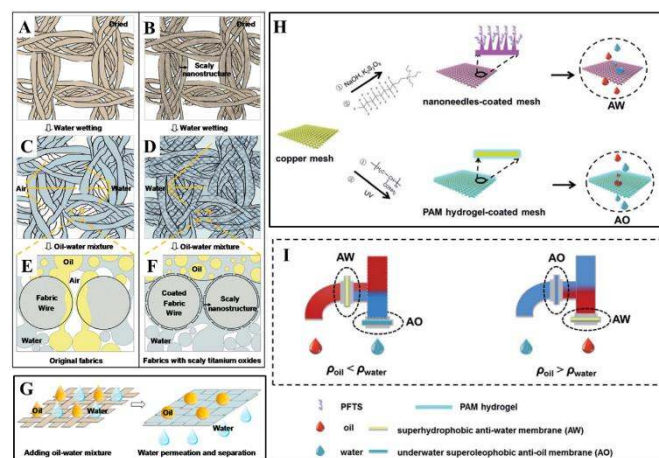


**Figure 16.** Schematic diagrams of wetting mechanism for the oil-water mixture separation on fabrics with two different films, viz. original film and scaly nanostructured film. A, C, E) Original film. B, D, F) Titanium-oxide-coated nanostructured film. A, B) Dried fabrics. C, D) Fabrics after water wetting. E, F) Cross-sectional analysis diagrams of the oil and water wetting process on fabrics with the original and titanium-oxide-coated nanostructured films. G) Schematic diagrams of the oil-water mixture separation process. Reproduced with permission.[163] Copyright 2015, American Chemical Society. H) Schematic and I) Setup of an integrated dual-membrane separation system. Reproduced with permission.[164] Copyright 2016, The Royal Society of Chemistry.

3.3.1.3 Stimuli-responsive wettability: Apart from the above main mechanisms of liquid penetration, stimuli-responsive wettability is worthy of attention. The simulation may come from surface tension,[165, 166] electric field,[167] light,[168, 169] pH,[170] and temperature.[171-173]

Manipulating the surface tension of nanofibrous membranes to lie between the intrinsic wetting thresholds (IWTs) of the two organic liquids to be separated, Wang et al. endowed the nanofibrous membranes with superlyophobicity and superlyophilicity for the two liquids, and thus successfully separated the liquids. As shown in Fig. 17A, when surface tensions of the membrane ($\gamma^{sv}$) is precisely manipulated to be $\gamma_{IWT}^{sv(A)} > \gamma^{sv} > \gamma_{IWT}^{sv(B)}$), the membrane is lyophobic for liquid A and lyophilic for liquid B. After roughing the membrane, the nanofibrous membranes can be endowed with superlyophobicity and superlyophilicity, respectively, thus enabling the successful separation of liquid A and liquid B. If $\gamma^{sv} > \gamma_{IWT}^{sv(A)}$, the membrane is lyophilic for the liquid (left, model of liquid A); whereas if $\gamma^{sv} < \gamma_{IWT}^{sv(B)}$, the membrane is lyophobic for the liquid (right, model of liquid B). This strategy is significant to separate any immiscible liquids efficiently and may lead to the development of membranes with a large capacity, high flux, and high selectivity for organic reactions or liquid extraction in chemical engineering.[166]

Utilizing symmetric poly(methyl methacrylate-b-N-isopropylacrylamide) (PMMA-b-PNIPAAm), Xue et al. endowed the block copolymer (BCP) membrane with reversible and switchable wettability between hydrophilic-oleophobicity and hydrophobic-oleophilicity in different temperature ranges. Utilizing the method of direct casting, they achieved the BCP-based steel mesh with a temperature-controlled dual switch that can regulate the access of oil or water. As shown in Fig. 17B, when the solution temperature is below the low critical value, intermolecular hydrogen bonds with water trigger and generate a hydrated and swollen PNIPAAm,

providing a high proportion of water content on the surface. Due to the hydrophilic behaviour of both PNIPAAm and PMMA, the entire surface is hydrophilic with water wetting, which will effectively block the penetration of oil. When the temperature is above the low critical value, intramolecular hydrogen bonds trigger and generate a dehydrated and collapsed PNIPAAm. So PNIPAAm is hydrophobic and PMMA stays hydrophilic. With increasing temperature, PNIPAAm shrinks, but still with a large surface area. Thus, the BCP membrane is hydrophobic. For underwater oil, PMMA is oil-preferred, while the partially dehydrated PNIPAAm is oil-repellent, and still possesses a high percentage of water. After the BCP are self-assembled into a stratified structure, PNIPAAm locates between the nanoscale hard walls of PMMA. The dehydration degree of PNIPAAm can be quite high with the participation of nanoscale PMMA, and then the nano PNIPAAm domains become more oleophilic. Thus, the BCP membrane is oleophilic. This mechanism can be applied into the film for the controllable oil-water separation.[172]
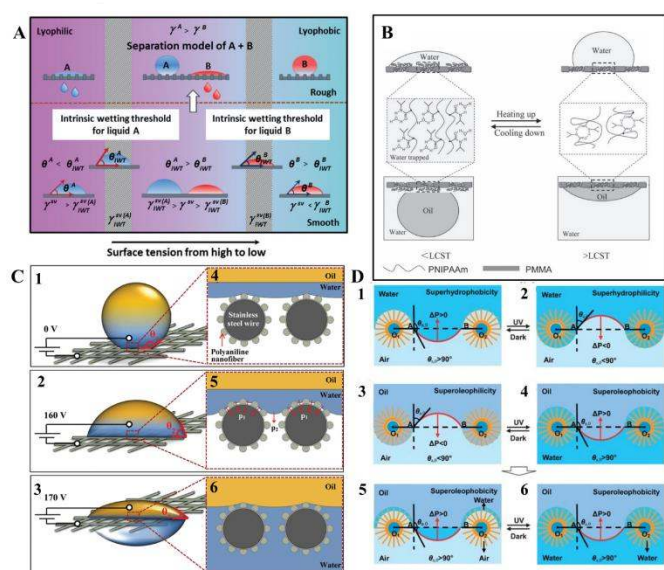


**Figure 17.** A) Schematic illustration of the mechanism of penetration by manipulating the surface tensions, Reproduced with permission.[166] Copyright 2015, Wiley-VCH Verlag GmbH & Co. KGaA, Weinheim. B) Mechanism diagram of reversible transformation for intermolecular hydrogen bonding and intramolecular hydrogen bonding, Reproduced with permission.[172] Copyright 2013, Wiley-VCH Verlag GmbH & Co. KGaA, Weinheim. C) Mechanism diagram of oil-water separation process on the polyaniline mesh induced by different electric fields, Reproduced with permission.[167] Copyright 2016, Wiley-VCH Verlag GmbH & Co. KGaA, Weinheim. D) Schematic mechanism diagrams of the photo-induced water-oil separation. Reproduced with permission.[169] Copyright 2012, The Royal Society of Chemistry.

Electric field was used by Zeng et al., they have achieved selective water penetration using a stainless-steel mesh. Such micro/nanoscale hierarchical-structured polyaniline mesh is superhydrophobic and underwater superoleophobic, covered with root-like polyaniline nanofibers. As shown in Fig. 17C, water of Cassie state can hardly penetrate the superhydrophobic mesh without applied voltage. Meanwhile, oil also keeps away from the mesh because of its underwater superoleophobicity. When the applied voltage is 160 V, the water-air interface starts to sag, then water can penetrate the mesh slightly with the electric capillary pressure (ECP) increasing, while oil still stays above the mesh. Once the applied voltage reaches 170 V, water of Cassie state transforms to Wenzel state and penetrates the mesh, whereas oil still keeps staying over the mesh due to its underwater superoleophobicity. Therefore, once the ECP exceeds the membrane hydrostatic pressure to water, the oil-water separation of

electric field induction will be realized, opening a possibility for controlled oil-water separation.[167]

Additionally, based on photo-induced mechanism, researchers have also developed controllable oil-water separation. Tian et al. fabricated a switchable superhydrophobic-superhydrophilic and underwater superoleophobic of aligned ZnO nanorod arrays membrane. Using this kind of material, they achieved superior controllability and separation efficiency for various oil-water mixtures in the oil-water-solid three-phase system. As shown in Fig. 17D, when the storage is in the dark, $\Delta P > 0$, water cannot penetrate the membrane in air. Under UV irradiation, $\Delta P < 0$, water will penetrate the membrane in air, and wet the nano-structured membrane completely. When oil is in the dark, $\Delta P < 0$, it will penetrate the membrane in air. Once UV is irradiated, $\Delta P > 0$, oil cannot penetrate the film in the oil-water-solid three-phase system.[169] This kind of membrane with the underwater superoleophobicity is able to prevent the oil pollution effectively, which is a great promise in photo-induced oil-water mixture treatment.

**3.3.2 Water penetration:** Apart from the separation of oil-water mixtures, single liquid penetration also draws many researcher's attention. Janus wettability is the main reason to cause single liquid penetration, such as water penetration.[174-177]

Based on 3-D cooperative hydrophobic-hydrophilic system, Cao et al. reported a continuous fog collector, consisting of hydrophilic cotton absorbent and hydrophobic copper mesh. As shown in Fig. 18A and C, when the fog droplets form on the single hydrophobic copper mesh, they condense on the copper mesh hump firstly and then start to grow gradually and coalesce with the adjacent condensates to form a bigger droplet, finally cover the mesh surface completely. While as for the Janus system, once the collected droplet contacts the hydrophilic backside (Fig. 18B and D), it would simultaneously penetrate through the system and vacate the area for new condensation. Such a mechanism not only allows continuous water collection, but also decreases the surface water re-evaporation rate. Such a Janus fog system (Fig. 18E and F) has been verified to be a continuous process for fog water harvesting.[174]

Additionally, using an electrospray method, Wu et al. successfully prepared a ''water diode'' membrane, comprised of hydrophobic polyurethane (PU) and hydrophilic cross-linked poly (vinyl alcohol) (c-PVA). Such device exhibits a distinct wettability difference and an excellent unidirectional water penetration functionality. Using this material, they found water can permeate spontaneously from its hydrophobic area to the hydrophilic area (Fig. 18G), but no occurrence of this permeation once the film is turned over (Fig. 18H). As illustrated in Fig. 18I, water droplets on the PU-upward hydrophobic area are under two opposing forces, one is hydrostatic pressure (HP), the other one is hydrophobic force (HF) which resists the water downward permeation provided by HP. With increasing water volume, the HP increases while the HF remains constant. As a result, water goes deeper. When the permeation depth reaches the PU membrane thickness, water will touch the lower hydrophilic c-PVA membrane, and continuous permeation will occur by the capillary force (CF) and the HP. But for the water droplets on the c-PVA-upward hydrophilic area, it spreads to a thin membrane with capillarity action. When the water droplet reaches the interface of c-PVA and PU, further water permeation will not occur due to the HF prevention provided by porous PU membrane.[177] Similar with Lin et al.'s investigation,[178] they found regulating the thickness of the film plays a crucial role in deciding the unidirectional water transport capability, which may benefit for the various applications of novel "smart" textiles.
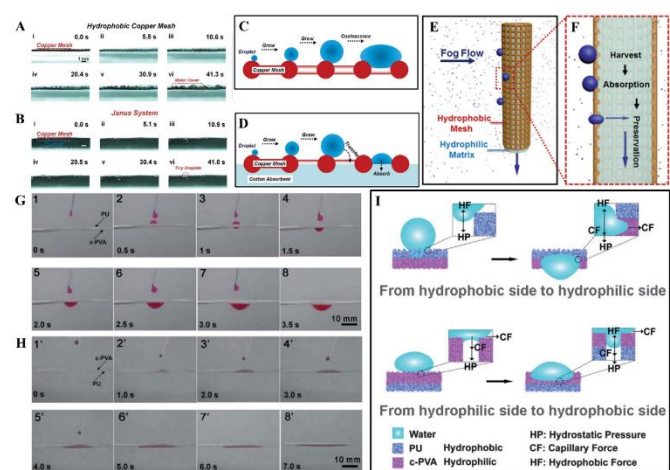
**Figure 18.** A-B) The fog harvesting dynamic process on A) a horizontal single hydrophobic copper mesh, B) Janus system, C-D) Schematic diagram about the process of condensate on C) copper mesh and D) Janus system, E) The front-view and F) the cross-section diagram for the fog harvesting process on the Janus collector, Reproduced with permission.[174] Copyright 2015, Wiley-VCH Verlag GmbH & Co. KGaA, Weinheim. G) Snapshots of water droplets penetration through the upward hydrophobic PU side. H) Snapshots of water droplets penetration through the upward hydrophilic c-PVA film side. I) Mechanism of unidirectional water penetration on a heterogeneous wettable composite film. Reproduced with permission.[177] Copyright 2012, The Royal Society of Chemistry.

# 4. Application of liquid mobility in energy and environment

## 4.1 Enhanced heat transfer

As a high-efficiency energy-transport strategy, vapor-liquid phase-change heat transfer has been applied in thermal management, air conditioning, power generation, and waste-heat exploitation etc. There are two common types of condensation, namely filmwise condensation and dropwise condensation. Dropwise condensation on the hydrophobic surfaces is typically ten times more efficient in phase-change heat transfer than filmwise condensation, resulting from the efficient coalescence-induced propelling, which can be realized through the released excess surface energy in the course of microdroplets coalescence without any external forces. Whereas as for filmwise condensation on the hydrophilic surfaces, gravity-induced shedding is the dominant mechanism but it is usually not efficient: only when the condensate diameter comes up to the capillary length, it can then slide off.[179]

Nowadays, researchers focus more attention on the enhancement of heat transfer. Based on the fabrication of materials (inorganic oxides, silicon, polymers, and metal etc.) with condensate microdroplet self-propelling ability, large breakthroughs have been made in enhancing heat transfer. Gao's group prepared surface of clustered copper hydroxide ribbed-nanoneedles to achieve over 125% enhancement in dropwise condensation heat transfer (DCHT) coefficient. Later on, they achieved over 89% enhancement in the DCHT coefficient on copper-based ultrathin nickel nanocone films. Utilizing the well-established top-down micro- and nanofabrication technologies, many researchers have managed to achieve the enhancement of heat transfer using silicon micro- or nanostructures (e.g., nanoneedles[180], nanocones[181], micropillars[182, 183] and micropyramids[184]), hierarchically structured porous aluminum,[48] copper oxide surfaces,[185] titanium-based surfaces,[30] and scalable graphene coatings[186].

## 4.2 Self-cleaning & Anti-fouling

Self-cleaning & anti-fouling technology has been developed since the late 20th century, and some achievements have been made by researchers and developed to practical applications. Inspired by lotus leaf, rice leaf, cicada wing, butterfly wing, snail shell, fish scale, shark skin, pitcher plant, and gecko, the self-cleaning & anti-fouling technology are very broad and have been applied in many fields varying from window glasses to solar cell panels.[6, 8, 12, 187-189] At present, self-cleaning & anti-fouling surfaces can be divided into several categories, i.e. superhydrophobic surface, superhydrophilic surface, hydrophilic & olephobic-in-water surface, and dry self-cleaning surface.[190] Special wettability and droplet mobility are crucial factor in deciding the efficiency of self-cleaning & anti-fouling.

For the superhydrophobic surfaces, the self-cleaning function is traditionally resulting from the removal of the contaminated particles by rolling water droplets, usually under an external force such as gravity. If the contaminants are removed autonomously by the condensate self-propelled jumping motion, driven by the released surface energy from the condensate microdroplets coalescence as discussed before, the self-cleaning will be more efficient.[7] Therefore, how to design the micro- or nano-construction of materials surface is crucial. Techniques to produce superhydrophobic surfaces not only need a rough surface but also with low surface energy. However, low surface energy matters, such as fluorosilicone polymers, fluoropolymers, are harmful to human beings and environment, and easily lose the functionality during application. Novel environmentally friendly materials are required in the future research. As for the superhydrophilic surfaces, it is mainly based on the special photo-induced properties viz. photocatalysis and photo-induced superhydrophilicity to achieve self-cleaning property through chemically breaking down organic dirt and mechanically washing away other dirt on the surface.[191] Different from the above-mentioned superhydrophobic and superhydrophilic surfaces, dry self-cleaning is an intrinsic property to nanostructured surface inspired from gecko setal, occurs by an energetic disequilibrium between the adhesive forces attracting a dirt particle to the substrate and those attracting the same particle to one or more spatula. Whereas once materials are fouled by oil, the hydrophilic & olephobic-in-water surface can efficiently resist the oil to penetrate through the self-functionalized wettability surface.

## 4.3 Anti-icing

Ice accumulation on solid surfaces is a common occurrence in winter, which can cause serious problems for road, aviation, cables, shipping and some energy equipment. In the past few decades, researchers have developed a variety of anti-icing techniques to reduce the formation of ice, and to reduce ice adhesion. A full process of freezing on a superwettability surface includes steps of self-jumping, bouncing, wetting in the liquid phase, and ice nucleating, bridging in the solid phase.

At present, researches on anti-icing coatings are focused on two general strategies, namely lotus leaf-like superhydrophobic coatings and slippery liquid-infused surfaces.[192] Recent studies have shown that surface ice nucleus adhesive force is closely related to surface wetting, as expressed in contact angle, receding angle, wetting hysteresis and dynamic hydrophobicity.[193-195] Generally, surface chemistry and morphology are combined to realize the required icephobicity.[196] Dipping method, vapor deposition method, spraying method are mostly utilized to achieve low surface energy. The second strategy, liquid-infused layered coatings, including the oil-infused slippery liquid-infused porous surface (SLIPS) and aqueous-infused SLIPS, have aroused a lot of attention since Aizenberg and co-

workers fabricated a slippery, ice-phobic surface on aluminium surfaces. SLIPS can not only significantly decrease water accumulation due to the timely sliding condensate droplets before freeze, but also easily remove the ice accretion and melted water through the action of gravity force at a low tilting angle.[197] However, due to the high coating porosity, the weak mechanical properties pose great constraints to the application of SLIPS. New strategies are necessary in the future research.

### 4.4 Water-harvesting

Water pollution and shortage of clear water have caused serious health and social problems in many countries. To obtain clean water, fog collection has attracted widespread attention in research in recent years. Technically, the process includes water condensation, coalescence, transportation, and storage.[198] Therefore, the mobility of water droplet plays a significant role in the efficiency of water-harvesting.

During the investigation on super-wettability in recent years, scholars have proposed many strategies to fabricate materials with fog-harvesting ability. Inspired by the spider silk, researchers have constructed a number of one-dimensional artificial spider silk through different methods,[199] such as dip-coating method, electro-dynamic method, micro-fluid method, fluid-coating method.[118-125, 200-208] Inspired by the cactus, various 1-D bio-inspired cactus structures have been fabricated,[198] using magnetic particle-assisted moulding method, chemical or electrochemical erosion method, electrospinning with sacrificial template method, mechanical punching, and template replica method.[209-221] For 2-D materials, researchers have developed a variety of technologies through biomimetic methods, such as photolithograph, mechanical micro-milling, composite technology, stimulus-trigger materials fabrication, and inkjet printing technology.[131, 222-226]

### 4.5 Oil-water separation

During oil exploitation and transportation, the occurrence of oil leakage and spill can seriously cause soil and water pollution, and then threaten the health of humans and other species. Therefore, how to effectively solve such problems has become a top priority in oil-water separation research. Currently, for the investigation of oil-water separation, researchers mainly focus on porous materials with special wettability, i.e., superhydrophobicity-superoleophilicity, superhydrophilicity-superoleophobicity, superhydrophilicity-underwater superoleophobicity and stimuli-responsive wettability.[227] Therefore, how to design the materials with special wettability is significant to the enhancement of the oil-water separation efficiency.

At present, scientists have designed various structure on various materials, such as textile,[134, 152] stainless steel mesh,[139, 149, 150, 153, 154, 157] copper mesh,[155, 164] sponges,[136, 137, 143] foams,[144, 151] wood[159] and hydrogels.[156, 158] Lai's group systematically investigated the fabrication on textile. Using a facile one-step hydrothermal strategy, they fabricated flower-like hierarchical $TiO_2$ micro/nanoparticles onto cotton fabric substrates, and successfully achieved the materials of functionality for self-cleaning, laundering durability, and oil/water separation.[228] Subsequently, they chose a facile and green dip-coating method to deposit an organically modified silica aerogel thin film onto the fabrics, followed by polydimethylsiloxane (PDMS) coating to obtain a highly robust porous network on the fibers with excellent anti-fouling, self-cleaning ability and highly efficient oil-water separation.[229] Furthermore, they improved the method to fabricate non-particle and friendly transparent surface, and likewise achieved excellent versatile oil-water separation.[230-232]

## 5. Conclusions

In summary, different types of liquid mobility on superwettable surfaces have been reviewed, including vertical motion, horizontal transportation and interfacial penetration based on materials with different wettability attributes. Attention has been focused on the mechanisms of liquid mobility, and the applications including enhancement of heat transfer coefficient, strengthening water-harvesting efficiency, suppressing or delaying ice formation, improving oil-water separation and self-cleaning capabilities.

Inspired by the bio-organisms with superwettabilities, there have been significant efforts to create synthetic materials and investigate factors that influence liquid mobility. Nevertheless, the field of directional liquid mobility is still in the early stage. At present, a main topic in the vertical liquid motion has been directional self-propelling: how to reduce the contact time on a superhydrophobic substrate while achieving directional, high-efficiency, and mechanically durable surface that can reduce energy consumption, circulation, wear, abrasion, and erosion. However, it remains challenging of how to fabricate micro- and nano-structures and at what length scale to drive the droplet bouncing on the substrate directional in a low and high temperature environment. Meanwhile, long-term durability of coatings, especially on those with surface textures, are questionable. Nowadays, significant advances in micro/nanotechnology and high-speed imaging, the movement detail (such as contact time, critical spreading diameter) of more microscopic droplets has been observed and the corresponding mechanisms with the phenomenon are gradually being revealed. Thus, how to relate the relevant parameters of liquid droplet movement behavior to existing hydrodynamic remains to be further investigated.

Nowadays, the intrinsic characteristics of the 1-D and 2-D materials for the transportation have been paid more attentions by researchers, including the wettability gradient, Janus wettability, and single wettability, but is still pending without uniform conclusions. At the present stage, controlling microdroplets transportation on micro- and nano- scale surface is very difficult to achieve, how to control and achieve precise droplet moving direction also need to be further improved. More investigations involve the droplets spontaneous movement, but only within ten centimeters distance, thus in order to expedite the application process in the industrial field, how to drive droplets to move faster with a long distance is significant, which should be achieved through combining more driving forces. Actually, despite the wettability and the micro/nano-structure have indispensable effects on the directional transportation, macro-structures should not be neglected, especially some 3-D materials which can be designed by 3-D printing and has attracted more and more attention. Based on the precise 3-D printed materials with excellent wettability design, maybe researchers can obtain more discoveries.

With regard to the liquid (water or oil) interface penetration on porous membranes, including oil-water penetration and water penetration, most of researches focus their behaviours on fabrics, foams, sponges, and polymer membranes which are rarely applied in industrial scale applications. Future investigation should be based on materials widely used in industry and their long-term durability. Besides, as for porous materials with micro-scale pore size, liquid interface penetration is difficult to be observed by high speed imaging experimentally. As for high-viscosity liquids, the speed of liquid penetration at interface will be low and hard to meet the industrial progress. Therefore, advanced fabrication and rational design for rapid liquid interface penetration should be considered. As for most of materials, coating is significant to improve the wettability of materials. However, coatings without annealing can be easily

damaged by mechanical force and chemical contamination. Long-chain fluorinated coatings, despite offering some of the highest water contact angles, are known to be carcinogenic. Therefore, development of cheap, fluorine-free, and robust coatings is of great interests.

Many seemingly great materials are limited in their practical applications either because of the challenge in scaling up or lack of standardized evaluation following international standards. For example, droplets of different sizes have been used by different research groups to measure the effectiveness of liquid mobility on super-wettability materials, comparing their effectiveness becomes a problem without using a unified test standard. Much more challenges have to be solved before practical applications because of the complexity in application involving physical (environmental humidity, pH value of solution, substrate temperature) productivity, and cost.

With the increasing population, consumption of natural resources and intensification of environmental pollution, environmental-friendly and low-cost way of harvesting clean water is a critical issue faced by human being. Research on liquid mobility on super-wettability materials will provide an answer to the challenge. In addition, smart and multifunctional materials should be paid more attention in the future. Especially, the mechanism of directional liquid mobility on super-wettability materials still remains to be verified and deserves further investigation. In the very near future, we are expecting to see more exciting achievements arising in the field of liquid mobility.

## Conflicts of interest

There are no conflicts to declare.

## Acknowledgements

## Notes and references

1    T. Young, *Philos. Trans. R. Soc. London*, 1805, **95**, 65-87.
2    A. B. D. Cassie and S. Baxter, *Trans. Faraday Soc.*, 1944, **40**, 546-551.
3    R. N. Wenzel, *Ind. Eng. Chem.*, 1936, **28**, 988-994.
4    R. N. Wenzel, *J. Phys. Colloid Chem.*, 1949, **53**, 1466-1467.
5    J. L. Rosano, Mem. Serv. Chim. Etat., 1951, 36.
6    W. Barthlott and C. Neinhuis, *Planta*, 1997, **202**, 1-8.
7    K. M. Wisdom, J. A. Watson, X. Qu, F. Liu, G. S. Watson and C. H. Chen, *Proc. Natl. Acad. Sci. USA*, 2013, **110**, 7992-7997.
8    Y. Zheng, X. Gao and L. Jiang, *Soft Matter*, 2007, **3**, 178-182.
9    G. D. Bixler and B. Bhushan, *Nanoscale*, 2014, **6**, 76-96.
10   X. Gao, X. Yan, X. Yao, L. Xu, K. Zhang, J. Zhang, B. Yang and L. Jiang, *Adv. Mater.*, 2007, **19**, 2213-2217.
11   X. Gao and L. Jiang, *Nature*, 2004, **432**, 36.
12   H. Chen, P. Zhang, L. Zhang, H. Liu, Y. Jiang, D. Zhang, Z. Han and L. Jiang, *Nature*, 2016, **532**, 85-89.
13   L. Rayleigh, *Proc. R. Soc. Lond.*, 1882, **34**.130
14   D. Richard, C. Clanet and D. Quéré, *Nature*, 2002, **417**, 811.
15   Y. Zheng, H. Bai, Z. Huang, X. Tian, F. Q. Nie, Y. Zhao, J. Zhai and L. Jiang, *Nature*, 2010, **463**, 640-643.
16   J. Ju, H. Bai, Y. Zheng, T. Zhao, R. Fang and L. Jiang, *Nat. Commun.*, 2012, **3**, 1247.
17   M. K. Chaudhury and G. M. Whitesides, *Science*, 1992, **256**, 1539-1541.
18   S. Daniel, M. K. Chaudhury and J. C. Chen, *Science*, 2001, **291**, 633-636.
19   C. Liu, Y. Xue, Y. Chen and Y. Zheng, *Sci. Rep.*, 2015, **5**, 17757.
20   L. Lorenceau and D. Qur, *J. Fluid Mech.*, 2004, **510**, 29-45.
21   M. Prakash, D. Quere and J. W. Bush, *Science*, 2008, **320**, 931-934.
22   A. R. Parker and C. R. Lawrence, *Nature*, 2001, **414**, 33-34.
23   K. C. Park, P. Kim, A. Grinthal, N. He, D. Fox, J. C. Weaver and J. Aizenberg, *Nature*, 2016, **531**, 78-82.
24   J. B. Boreyko and C. H. Chen, *Phys. Rev. Lett.*, 2009, **103**, 184501.
25   J. Feng, Z. Qin and S. Yao, *Langmuir*, 2012, **28**, 6067-6075.
26   Y. Lai, X. Gao, H. Zhuang, J. Huang, C. Lin and L. Jiang, *Adv. Mater.*, 2009, **21**, 3799-3803.
27   R. Raj, R. Enright, Y. Zhu, S. Adera and E. N. Wang, *Langmuir*, 2012, **28**, 15777-15788.
28   W. Choi, A. Tuteja, J. M. Mabry, R. E. Cohen and G. H. McKinley, *J. Colloid Interf. Sci.*, 2009, **339**, 208-216.
29   W. Li and A. Amirfazli, *J. Colloid Interf. Sci.*, 2005, **292**, 195-201.
30   S. Zhang, J. Huang, Y. Tang, S. Li, M. Ge, Z. Chen, K. Zhang and Y. Lai, *Small*, 2017, **13**, 1600687.
31   R. Enright, N. Miljkovic, J. Sprittles, K. Nolan, R. Mitchell and E. N. Wang, *ACS Nano*, 2014, **8**, 10352-10362.
32   F. Liu, G. Ghigliotti, J. J. Feng and C.-H. Chen, *J. Fluid Mech.*, 2014, **752**, 39-65.
33   X. Liu, P. Cheng and X. Quan, *Int. J. Heat Mass Tran.*, 2014, **73**, 195-200.
34   F.-C. Wang, F. Yang and Y.-P. Zhao, *Appl. Phys. Lett.*, 2011, **98**, 053112.
35   J. Tian, J. Zhu, H. Y. Guo, J. Li, X. Q. Feng and X. Gao, *J. Phys. Chem. Lett.*, 2014, **5**, 2084-2088.
36   Y. Nam, H. Kim and S. Shin, *Appl. Phys. Lett.*, 2013, **103**, 161601.
37   R. Enright, N. Miljkovic, A. Al-Obeidi, C. V. Thompson and E. N. Wang, *Langmuir*, 2012, **28**, 14424-14432.
38   Y. Cho, G. Kim, Y. Cho, S. Y. Lee, H. Minsky, K. T. Turner, D. S. Gianola and S. Yang, *Adv. Mater.*, 2015, **27**, 7788-7793.
39   X. Jin, X. Zhang, Y. Peng, M. Cao, H. Liu, X. Pei, K. Liu and L. Jiang, *Adv. Eng. Mater.*, 2015, **17**, 961-968.
40   J. Li, W. Zhang, Y. Luo, J. Zhu and X. Gao, *ACS Appl. Mater. Inter.*, 2015, **7**, 18206-18210.
41   J. Liu, H. Guo, B. Zhang, S. Qiao, M. Shao, X. Zhang, X. Q. Feng, Q. Li, Y. Song, L. Jiang and J. Wang, *Angew. Chem. Int. Ed.*, 2016, **55**, 4265-4269.
42   Y. Luo, J. Li, J. Zhu, Y. Zhao and X. Gao, *Angew. Chem. Int. Ed.*, 2015, **54**, 4876-4879.
43   B. Mondal, M. Mac Giolla Eain, Q. Xu, V. M. Egan, J. Punch and A. M. Lyons, *ACS Appl. Mater. Inter.*, 2015, **7**, 23575-23588.
44   W. Zhang, G. Lin, J. Li, H. Xue, Y. Luo and X. Gao, *Adv. Mater. Interfaces*, 2015, **2**, 1500238.
45   Y. Zhao, Y. Luo, J. Li, F. Yin, J. Zhu and X. Gao, *ACS Appl. Mater. Inter.*, 2015, **7**, 11079-11082.
46   Y. Cho, T. S. Shim and S. Yang, *Adv. Mater.*, 2016, **28**, 1433-1439.

47   M. He, Q. Zhang, X. Zeng, D. Cui, J. Chen, H. Li, J. Wang and Y. Song, *Adv. Mater.*, 2013, **25**, 2291-2295.

48   M. He, X. Zhou, X. Zeng, D. Cui, Q. Zhang, J. Chen, H. Li, J. Wang, Z. Cao, Y. Song and L. Jiang, *Soft Matter*, 2012, **8**, 6680-6683.

49   C. Lv, P. Hao, Z. Yao, Y. Song, X. Zhang and F. He, *Appl. Phys. Lett.*, 2013, **103**, 021601.

50   J. C. Bird, R. Dhiman, H. M. Kwon and K. K. Varanasi, *Nature*, 2013, **503**, 385-388.

51   A.-L. Biance, F. Chevy, C. Clanet, G. Lagubeau and D. Quéré, *J. Fluid Mech.*, 2006, **554**, 47-66.

52   J. E. Field, *Wear,* 1999, **233-235**, 1-12.

53   C. Hao, Y. Liu, X. Chen, J. Li, M. Zhang, Y. Zhao and Z. Wang, *Small*, 2016, **12**, 1825-1839.

54   C. Josserand and S. T. Thoroddsen, *Annu. Rev. Fluid Mech.*, 2016, **48**, 365-391.

55   R. Rioboo, C. Tropea and M. Marengo, *Atomization Spray.*, 2001, **11**, 155-165.

56   T. Tran, H. J. Staat, A. Prosperetti, C. Sun and D. Lohse, *Phys. Rev. Lett.*, 2012, **108**, 036101.

57   L. Xu, W. W. Zhang and S. R. Nagel, *Phys. Rev. Lett.*, 2005, **94**, 184505.

58   A. L. Yarin, *Annu. Rev. Fluid Mech.*, 2006, **38**, 159-192.

59   S. Schiaffino and A. A. Sonin, *Phys. Fluids*, 1997, **9**, 3172-3187.

60   X. Deng, F. Schellenberger, P. Papadopoulos, D. Vollmer and H. J. Butt, *Langmuir*, 2013, **29**, 7847-7856.

61   D. Richard and D. Quéré, *EPL-Europhys. Lett.*, 2000, **50**, 769-775.

62   D. B. van Dam and C. Le Clerc, *Phys. Fluids*, 2004, **16**, 3403-3414.

63   I. S. Bayer and C. M. Megaridis, *J. Fluid Mech.*, 2006, **558**, 415-449.

64   C. Clanet, C. BéGuin, D. Richard and D. Quéré, *J. Fluid Mech.*, 2004, **517**, 199-208.

65   J. de Ruiter, R. Lagraauw, D. van den Ende and F. Mugele, *Nat. Phys.*, 2014, **11**, 48-53.

66   A. Mongruel, V. Daru, F. Feuillebois and S. Tabakova, *Phy. Fluids*, 2009, **21**, 032101.

67   R. D. Schroll, C. Josserand, S. Zaleski and W. W. Zhang, *Phys. Rev. Lett.*, 2010, **104**, 034504.

68   C. W. Visser, Y. Tagawa, C. Sun and D. Lohse, *Soft Matter*, 2012, **8**, 10732-10737.

69   S. Chandra and C. T. Avedisian, *Proc. R. Soc. Lond. A*, 1991, **432**, 13-41.

70   M. Rein, *Fluid Dyn. Res.*, 1993, **12**, 61-93.

71   M. Pasandideh-Fard, Y. M. Qiao, S. Chandra and J. Mostaghimi, *Phys. Fluids*, 1996, **8**, 650-659.

72   K. Okumura, F. Chevy, D. Richard, D.Quéré and C. Clanet, *Europhys. Lett.*, 2003, **62**, 237-243.

73   D. Bartolo, C. Josserand and D. Bonn, *J. Fluid Mech.*, 2005, **545**, 329-338.

74   F. E. C. Culick, *J. Appl. Phys.*, 1960, **31**, 1128-1129.

75   G. Taylor, *P. Roy. Soc. A-Math. Phy.*, 1959, **253**, 313-321.

76   X. Li, X. Ma and Z. Lan, *Langmuir*, 2010, **26**, 4831-4838.

77   Y. Shen, J. Tao, H. Tao, S. Chen, L. Pan and T. Wang, *Appl. Phys. Lett.*, 2015, **107**, 111604.

78   A. Gauthier, S. Symon, C. Clanet and D. Quere, *Nat. Commun.*, 2015, **6**, 8001.

79   Y. Liu, L. Moevius, X. Xu, T. Qian, J. M. Yeomans and Z. Wang, *Nat. Phys.*, 2014, **10**, 515-519.

80   Y. Liu, M. Andrew, J. Li, J. M. Yeomans and Z. Wang, *Nat. Commun.*, 2015, **6**, 10034.

81   T. Deng, K. K. Varanasi, M. Hsu, N. Bhate, C. Keimel, J. Stein and M. Blohm, *Appl. Phys. Lett.*, 2009, **94**, 133109.

82   D. Bartolo, F. Bouamrirene, É. Verneuil, A. Buguin, P.

Silberzan and S. Moulinet, *EPL-Europhys. Lett.* , 2006, **74**, 299-305.

83   S. Dash, M. T. Alt and S. V. Garimella, *Langmuir*, 2012, **28**, 9606-9615.

84   D. Hee Kwon and S. Joon Lee, *Appl. Phys. Lett.*, 2012, **100**, 171601.

85   J. Hyväluoma and J. Timonen, *EPL-Europhys. Lett.*, 2008, **83**, 64002.

86   Y. C. Jung and B. Bhushan, *Langmuir*, 2008, **24**, 6262-6269.

87   H. M. Kwon, A. T. Paxson, K. K. Varanasi and N. A. Patankar, *Phys. Rev. Lett.*, 2011, **106**, 036102.

88   A. Lafuma and D. Quéré, *Nat. Mater.*, 2003, **2**, 457-460.

89   M. Reyssat, A. Pépin, F. Marty, Y. Chen and D. Quéré, *EPL-Europhys. Lett.*, 2006, **74**, 306-312.

90   M. Reyssat, D. Richard, C. Clanet and D. Quéré, *Faraday Discuss.*, 2010, **146**, 19-33.

91   Z. Wang, C. Lopez, A. Hirsa and N. Koratkar, *Appl. Phys. Lett.*, 2007, **91**, 023105.

92   M. K. Chaudhury and G. M. Whitesides, *Science*, 1992, **256**, 1539-1541.

93   K. H. Chu, R. Xiao and E. N. Wang, *Nat. Mater.*, 2010, **9**, 413-417.

94   B. A. Malouin, N. A. Koratkar, A. H. Hirsa and Z. Wang, *Appl. Phys. Lett.*, 2010, **96**, 234103.

95   M. Reyssat, F. Pardo and D. Quéré, *EPL-Europhys. Lett.*, 2009, **87**, 36003.

96   J. Wu, R. Ma, Z. Wang and S. Yao, *Appl. Phys. Lett.*, 2011, **98**, 204104.

97   G. Lagubeau, M. Le Merrer, C. Clanet and D. Quéré, *Nat. Phys.*, 2011, **7**, 395-398.

98   R. L. Agapov, J. B. Boreyko, D. P. Briggs, B. R. Srijanto, S. T. Retterer, C. P. Collier and N. V. Lavrik, *ACS Nano*, 2014, **8**, 860-867.

99   J. Li, Y. Hou, Y. Liu, C. Hao, M. Li, M. K. Chaudhury, S. Yao and Z. Wang, *Nat. Phys.*, 2016, **12**, 606-612.

100  D. A. del Cerro, A. G. Marin, G. R. Romer, B. Pathiraj, D. Lohse and A. J. Huis in 't Veld, *Langmuir*, 2012, **28**, 15106-15110.

101  T. Tran, H. J. J. Staat, A. Susarrey-Arce, T. C. Foertsch, A. van Houselt, H. J. G. E. Gardeniers, A. Prosperetti, D. Lohse and C. Sun, *Soft Matter*, 2013, **9**, 3272-3282.

102  R. C. van der Veen, M. H. Hendrix, T. Tran, C. Sun, P. A. Tsai and D. Lohse, *Soft Matter*, 2014, **10**, 3703-3707.

103  H. Nair, H. J. Staat, T. Tran, A. van Houselt, A. Prosperetti, D. Lohse and C. Sun, *Soft Matter*, 2014, **10**, 2102-2109.

104  R. P. Sahu, S. Sinha-Ray, A. L. Yarin and B. Pourdeyhimi, *Soft Matter*, 2012, **8**, 3957-3970.

105  C. M. Weickgenannt, Y. Zhang, S. Sinha-Ray, I. V. Roisman, T. Gambaryan-Roisman, C. Tropea and A. L. Yarin, *Phys. Rev. E* 2011, **84**, 036310.

106  H. Kim, B. Truong, J. Buongiorno and L.-W. Hu, *Appl. Phys. Lett.*, 2011, **98**, 083121.

107  C. Kruse, T. Anderson, C. Wilson, C. Zuhlke, D. Alexander, G. Gogos and S. Ndao, *Langmuir*, 2013, **29**, 9798-9806.

108  H. M. Kwon, J. C. Bird and K. K. Varanasi, *Appl. Phys. Lett.*, 2013, **103**, 201601.

109  T. Zhang, J. Wang, L. Chen, J. Zhai, Y. Song and L. Jiang, *Angew. Chem. Int. Ed.*, 2011, **50**, 5311-5314.

110  T. Baier, G. Dupeux, S. Herbert, S. Hardt and D. Quere, *Phys. Rev. E*, 2013, **87**, 021001.

111  G. Dupeux, M. Le Merrer, G. Lagubeau, C. Clanet, S. Hardt and D. Quéré, *EPL-Europhys. Lett.*, 2011, **96**, 58001.

112  H. Linke, B. J. Aleman, L. D. Melling, M. J. Taormina, M. J. Francis, C. C. Dow-Hygelund, V. Narayanan, R. P. Taylor and A. Stout, *Phys. Rev. Lett.*, 2006, **96**, 154502.

113  Á. G. Marín, D. Arnaldo del Cerro, G. R. B. E. Römer, B.

Pathiraj, A. Huis in 't Veld and D. Lohse, *Phys. Fluids*, 2012, **24**, 122001.

114 J. T. Ok, E. Lopez-Oña, D. E. Nikitopoulos, H. Wong and S. Park, *Microfluid. Nanofluid.*, 2010, **10**, 1045-1054.

115 A. Wurger, *Phys. Rev. Lett.*, 2011, **107**, 164502.

116 R. L. Agapov, J. B. Boreyko, D. P. Briggs, B. R. Srijanto, S. T. Retterer, C. P. Collier and N. V. Lavrik, *Nanoscale*, 2014, **6**, 9293-9299.

117 C. Liu, J. Ju, J. Ma, Y. Zheng and L. Jiang, *Adv. Mater.*, 2014, **26**, 6086-6091.

118 H. Bai, X. Tian, Y. Zheng, J. Ju, Y. Zhao and L. Jiang, *Adv. Mater.*, 2010, **22**, 5521-5525.

119 H. Bai, J. Ju, R. Sun, Y. Chen, Y. Zheng and L. Jiang, *Adv. Mater.*, 2011, **23**, 3708-3711.

120 H. Bai, R. Sun, J. Ju, X. Yao, Y. Zheng and L. Jiang, *Small*, 2011, **7**, 3429-3433.

121 X. Tian, Y. Chen, Y. Zheng, H. Bai and L. Jiang, *Adv. Mater.*, 2011, **23**, 5486-5491.

122 Y. Chen, L. Wang, Y. Xue, Y. Zheng and L. Jiang, *Soft Matter*, 2012, **8**, 11450-11454.

123 Y. Hou, Y. Chen, Y. Xue, L. Wang, Y. Zheng and L. Jiang, *Soft Matter*, 2012, **8**, 11236-11239.

124 Y. Hou, Y. Chen, Y. Xue, Y. Zheng and L. Jiang, *Langmuir*, 2012, **28**, 4737-4743.

125 Y. Chen, L. Wang, Y. Xue, L. Jiang and Y. Zheng, *Sci. Rep.*, 2013, **3**, 02927.

126 D. A. Edwards, H. Brenner and K. T. Wasan., *Interfacial Transport Processes and Rheology*, Elsevier, Boston, Mass., USA, 1991.

127 O. Bliznyuk, H. P. Jansen, E. S. Kooij, H. J. Zandvliet and B. Poelsema, *Langmuir*, 2011, **27**, 11238-11245.

128 H. Wu, K. Zhu, B. Cao, Z. Zhang, B. Wu, L. Liang, G. Chai and A. Liu, *Soft Matter*, 2017, **13**, 2995-3002.

129 A. Ghosh, R. Ganguly, T. M. Schutzius and C. M. Megaridis, *Lab Chip*, 2014, **14**, 1538-1550.

130 D. Hong, W. K. Cho, B. Kong and I. S. Choi, *Langmuir*, 2010, **26**, 15080-15083.

131 H. Bai, L. Wang, J. Ju, R. Sun, Y. Zheng and L. Jiang, *Adv. Mater.*, 2014, **26**, 5025-5030.

132 H. Chen, L. Zhang, P. Zhang, D. Zhang, Z. Han and L. Jiang, *Small*, 2017, **13**, 1601676.

133 C. Li, N. Li, X. Zhang, Z. Dong, H. Chen and L. Jiang, *Angew. Chem. Int. Ed.*, 2016, **55**, 14988-14992.

134 F. Guo, Q. Wen, Y. Peng and Z. Guo, *J. Mater. Chem. A*, 2017, **5**, 21866-21874.

135 L. Hu, S. Gao, Y. Zhu, F. Zhang, L. Jiang and J. Jin, *J. Mater. Chem. A*, 2015, **3**, 23477-23482.

136 Z. Kong, J. Wang, X. Lu, Y. Zhu and L. Jiang, *Nano Res.*, 2017, **10**, 1756-1766.

137 J. Li, L. Shi, Y. Chen, Y. Zhang, Z. Guo, B.-l. Su and W. Liu, *J. Mater. Chem.*, 2012, **22**, 9774-9781.

138 H. Liu, C.-Y. Cao, F.-F. Wei, P.-P. Huang, Y.-B. Sun, L. Jiang and W.-G. Song, *J. Mater. Chem. A*, 2014, **2**, 3557-3562.

139 Y. Lu, S. Sathasivam, J. Song, F. Chen, W. Xu, C. J. Carmalt and I. P. Parkin, *J. Mater. Chem. A*, 2014, **2**, 11628-11634.

140 J. Song, S. Huang, Y. Lu, X. Bu, J. E. Mates, A. Ghosh, R. Ganguly, C. J. Carmalt, I. P. Parkin, W. Xu and C. M. Megaridis, *ACS Appl. Mater. Interfaces*, 2014, **6**, 19858-19865.

141 J. Song, Y. Lu, J. Luo, S. Huang, L. Wang, W. Xu and I. P. Parkin, *Adv. Mater. Interfaces*, 2015, **2**, 1500350.

142 D. Tian, X. Zhang, X. Wang, J. Zhai and L. Jiang, *Phys. Chem. Chem. Phys.*, 2011, **13**, 14606-14610.

143 B. Wang, J. Li, G. Wang, W. Liang, Y. Zhang, L. Shi, Z. Guo and W. Liu, *ACS Appl. Mater. Interfaces*, 2013, **5**, 1827-

1839.

144 Z. L. Xiyao Zhang , Kesong Liu , Lei Jiang, *Adv. Funct. Mater.* , 2013, **23**, 2881-2886.

145 Z. Xu, L. Wang, C. Yu, K. Li, Y. Tian and L. Jiang, *Adv. Funct. Mater.*, 2018, **28**, 1703970.

146 Q. Zhang, Y. Cao, N. Liu, W. Zhang, Y. Chen, X. Lin, Y. Wei, L. Feng and L. Jiang, *J. Mater. Chem. A*, 2016, **4**, 18128-18133.

147 W. Zhang, Z. Shi, F. Zhang, X. Liu, J. Jin and L. Jiang, *Adv. Mater.*, 2013, **25**, 2071-2076.

148 T. Zhao, D. Zhang, C. Yu and L. Jiang, *ACS Appl. Mater. Interfaces*, 2016, **8**, 24186-24191.

149 Y. Chen, N. Wang, F. Guo, L. Hou, J. Liu, J. Liu, Y. Xu, Y. Zhao and L. Jiang, *J. Mater. Chem. A*, 2016, **4**, 12014-12019.

150 Y. Dong, J. Li, L. Shi, X. Wang, Z. Guo and W. Liu, *Chem. Commun.*, 2014, **50**, 5586-5589.

151 Y. Li, X. Zheng, Z. Yan, D. Tian, J. Ma, X. Zhang and L. Jiang, *ACS Appl. Mater. Interfaces*, 2017, **9**, 29177-29184.

152 N. Liu, R. Qu, Y. Chen, Y. Cao, W. Zhang, X. Lin, Y. Wei, L. Feng and L. Jiang, *Nanoscale*, 2016, **8**, 18558-18564.

153 N. Liu, W. Zhang, X. Li, R. Qu, Q. Zhang, Y. Wei, L. Feng and L. Jiang, *J. Mater. Chem. A*, 2017, **5**, 15822-15827.

154 Q. Ma, H. Cheng, Y. Yu, Y. Huang, Q. Lu, S. Han, J. Chen, R. Wang, A. G. Fane and H. Zhang, *Small*, 2017, **13**, 1700391.

155 J. Song, S. Li, C. Zhao, Y. Lu, D. Zhao, J. Sun, T. Roy, C. J. Carmalt, X. Deng and I. P. Parkin, *Nanoscale*, 2018, **10**, 1920-1929.

156 C. Teng, C. Lu, G. Ren, Y. Zhu, M. Wan and L. Jiang, *Adv. Mater. Interfaces*, 2014, **1**, 1400099.

157 Q. Wen, J. Di, L. Jiang, J. Yu and R. Xu, *Chem. Sci.*, 2013, **4**, 591-595.

158 Z. Xue, S. Wang, L. Lin, L. Chen, M. Liu, L. Feng and L. Jiang, *Adv. Mater.*, 2011, **23**, 4270-4273.

159 J. Yong, F. Chen, J. Huo, Y. Fang, Q. Yang, H. Bian, W. Li, Y. Wei, Y. Dai and X. Hou, *ACS Omega*, 2018, **3**, 1395-1402.

160 Z. Yu, F. F. Yun, Z. Gong, Q. Yao, S. Dou, K. Liu, L. Jiang and X. Wang, *J. Mater. Chem. A*, 2017, **5**, 10821-10826.

161 F. Zhang, W. B. Zhang, Z. Shi, D. Wang, J. Jin and L. Jiang, *Adv. Mater.*, 2013, **25**, 4192-4198.

162 W. Zhang, Y. Zhu, X. Liu, D. Wang, J. Li, L. Jiang and J. Jin, *Angew. Chem. Int. Ed.*, 2014, **53**, 856-860.

163 X. Zheng, Z. Guo, D. Tian, X. Zhang, W. Li and L. Jiang, *ACS Appl. Mater. Interfaces*, 2015, **7**, 4336-4343.

164 J. Liu, L. Wang, F. Guo, L. Hou, Y. Chen, J. Liu, N. Wang, Y. Zhao and L. Jiang, *J. Mater. Chem. A*, 2016, **4**, 4365-4370.

165 J. Liu, L. Wang, N. Wang, F. Guo, L. Hou, Y. Chen, J. Liu, Y. Zhao and L. Jiang, *Small*, 2017, **13**, 1600499.

166 L. Wang, Y. Zhao, Y. Tian and L. Jiang, *Angew. Chem. Int. Ed.*, 2015, **54**, 14732-14737.

167 X. Zheng, Z. Guo, D. Tian, X. Zhang and L. Jiang, *Adv. Mater. Interfaces*, 2016, **3**, 1600461.

168 L. Hu, S. Gao, X. Ding, D. Wang, J. Jiang, J. Jin and L. Jiang, *ACS Nano*, 2015, **9**, 4835-4842.

169 D. Tian, X. Zhang, Y. Tian, Y. Wu, X. Wang, J. Zhai and L. Jiang, *J. Mater. Chem.*, 2012, **22**, 19652-19657.

170 B. Wang and Z. Guo, *Chem. Commun.*, 2013, **49**, 9416-9418.

171 R. Ou, J. Wei, L. Jiang, G. P. Simon and H. Wang, *Environ. Sci. Technol.*, 2016, **50**, 906-914.

172 B. Xue, L. Gao, Y. Hou, Z. Liu and L. Jiang, *Adv. Mater.*, 2013, **25**, 273-277.

173 W. Song, F. Xia, Y. Bai, F. Liu, T. Sun and L. Jiang, *Langmuir* 2007, **23**, 327-331.

174 M. Cao, J. Xiao, C. Yu, K. Li and L. Jiang, *Small*, 2015, **11**, 4379-4384.

175 J. Chen, Y. Liu, D. Guo, M. Cao and L. Jiang, *Chem.*

*Commun.*, 2015, **51**, 11872-11875.

176    X. Tian, H. Jin, J. Sainio, R. H. A. Ras and O. Ikkala, *Adv. Funct. Mater.*, 2014, **24**, 6023-6028.

177    J. Wu, N. Wang, L. Wang, H. Dong, Y. Zhao and L. Jiang, *Soft Matter*, 2012, **8**, 5996-5999.

178    C. Zeng, H. Wang, H. Zhou and T. Lin, *Adv. Mater. Interfaces*, 2016, **3**, 1600036.

179    X. Gong, X. Gao and L. Jiang, *Adv. Mater.*, 2017, **29**, 1703002.

180    K. Rykaczewski, W. A. Osborn, J. Chinn, M. L. Walker, J. H. J. Scott, W. Jones, C. Hao, S. Yao and Z. Wang, *Soft Matter*, 2012, **8**, 8786-8794.

181    K.-C. Park, H. J. Choi, C.-H. Chang, R. E. Cohen, G. H. McKinley and G. Barbastathis, *ACS Nano*, 2012, **6**, 3789-3799.

182    K. Rykaczewski, A. T. Paxson, S. Anand, X. Chen, Z. Wang and K. K. Varanasi, *Langmuir*, 2013, **29**, 881-891.

183    R. Xiao, N. Miljkovic, R. Enright and E. N. Wang, *Sci. Rep.*, 2013, **3**, 01988.

184    X. Chen, J. Wu, R. Ma, M. Hua, N. Koratkar, S. Yao and Z. Wang, *Adv. Funct. Mater.*, 2011, **21**, 4617-4623.

185    N. Miljkovic, R. Enright, Y. Nam, K. Lopez, N. Dou, J. Sack and E. N. Wang, *Nano Lett.*, 2013, **13**, 179-187.

186    D. J. Preston, D. L. Mafra, N. Miljkovic, J. Kong and E. N. Wang, *Nano Lett.*, 2015, **15**, 2902-2909.

187    S. G. Lee, H. S. Lim, D. Y. Lee, D. Kwak and K. Cho, *Adv. Funct. Mater.*, 2013, **23**, 547-553.

188    E. P. Ivanova, J. Hasan, H. K. Webb, V. K. Truong, G. S. Watson, J. A. Watson, V. A. Baulin, S. Pogodin, J. Y. Wang, M. J. Tobin, C. Lobbe and R. J. Crawford, *Small*, 2012, **8**, 2489-2494.

189    W. R. Hansen and K. Autumn, *Proc. Natl. Acad. Sci. USA*, 2005, **102**, 385-389.

190    K. Liu and L. Jiang, *Annu. Rev. Mater. Res.*, 2012, **42**, 231-263.

191    I. P. Parkin and R. G. Palgrave, *J. Mater. Chem.*, 2005, **15**, 1689-1695.

192    S. Zhang, J. Huang, Y. Cheng, H. Yang, Z. Chen and Y. Lai, *Small*, 2017, **13**, 1701867.

193    S. A. Kulinich and M. Farzaneh, *Langmuir*, 2009, **25**, 8854-8856.

194    A. Dotan, H. Dodiuk, C. Laforte and S. Kenig, *J. Adhes. Sci. Technol.*, 2009, **23**, 1907-1915.

195    A. J. Meuler, J. D. Smith, K. K. Varanasi, J. M. Mabry, G. H. McKinley and R. E. Cohen, *ACS Appl. Mater. Interfaces*, 2010, **2**, 3100-3110.

196    A. J. Meuler, G. H. Mckinley and R. E. Cohen, *ACS Nano*, 2010, **4**, 7048-7052.

197    P. Kim, T.-S. Wong, J. Alvarenga, M. J. Kreder, W. E. Adorno-Martinez and J. Aizenberg, *ACS Nano*, 2012, **6**, 6569-6577.

198    S. Zhang, J. Huang, Z. Chen and Y. Lai, *Small*, 2017, **13**, 1602992.

199    J. Ju, Y. Zheng and L. Jiang, *Accounts Chem. Res.*, 2014, **47**, 2342-2352.

200    Y. Chen, D. Li, T. Wang and Y. Zheng, *Sci. Rep.*, 2016, **6**, 19978.

201    H. Dong, N. Wang, L. Wang, H. Bai, J. Wu, Y. Zheng, Y. Zhao and L. Jiang, *Chemphyschem*, 2012, **13**, 1153-1156.

202    H. Dong, Y. Zheng, N. Wang, H. Bai, L. Wang, J. Wu, Y. Zhao and L. Jiang, *Adv. Mater. Interfaces*, 2016, **3**, 1500831.

203    M. Du, Y. Zhao, Y. Tian, K. Li and L. Jiang, *Small*, 2016, **12**, 1000-1005.

204    X. H. He, W. Wang, Y. M. Liu, M. Y. Jiang, F. Wu, K. Deng, Z. Liu, X. J. Ju, R. Xie and L. Y. Chu, *ACS Appl. Mater. Interfaces*, 2015, **7**, 17471-17481.

205    Z. Huang, Y. Chen, Y. Zheng and L. Jiang, *Soft Matter*, 2011, **7**, 9468-9473.

206    A. Nandakumar, R. Truckenmuller, M. Ahmed, F. Damanik, D. R. Santos, N. Auffermann, J. de Boer, P. Habibovic, C. van Blitterswijk and L. Moroni, *Small*, 2013, **9**, 3405-3409.

207    X. Tian, H. Bai, Y. Zheng and L. Jiang, *Adv. Funct. Mater.*, 2011, **21**, 1398-1402.

208    L. Zhao, C. Song, M. Zhang and Y. Zheng, *Chem. Commun.*, 2014, **50**, 10651-10654.

209    F. Bai, J. Wu, G. Gong and L. Guo, *Adv. Sci.*, 2015, **2**, 1500047.

210    M. Cao, J. Ju, K. Li, S. Dou, K. Liu and L. Jiang, *Adv. Funct. Mater.*, 2014, **24**, 3235-3240.

211    A. Davis, E. Mele, J. A. Heredia-Guerrero, I. S. Bayer and A. Athanassiou, *J. Mater. Chem. A*, 2015, **3**, 23821-23828.

212    X. Heng, M. Xiang, Z. Lu and C. Luo, *ACS Appl. Mater. Interfaces*, 2014, **6**, 8032-8041.

213    J. Ju, K. Xiao, X. Yao, H. Bai and L. Jiang, *Adv. Mater.*, 2013, **25**, 5937-5942.

214    J. Ju, X. Yao, S. Yang, L. Wang, R. Sun, Y. He and L. Jiang, *Adv. Funct. Mater.*, 2014, **24**, 6933-6938.

215    K. Li, J. Ju, Z. Xue, J. Ma, L. Feng, S. Gao and L. Jiang, *Nat. Commun.*, 2013, **4**, 2276.

216    E. Mele, I. S. Bayer, G. Nanni, J. A. Heredia-Guerrero, R. Ruffilli, F. Ayadi, L. Marini, R. Cingolani and A. Athanassiou, *Langmuir*, 2014, **30**, 2896-2902.

217    E. Mele, J. A. Heredia-Guerrero, I. S. Bayer, G. Ciofani, G. G. Genchi, L. Ceseracciu, A. Davis, E. L. Papadopoulou, M. J. Barthel, L. Marini, R. Ruffilli and A. Athanassiou, *Sci. Rep.*, 2015, **5**, 14019.

218    K. A. Moga, L. R. Bickford, R. D. Geil, S. S. Dunn, A. A. Pandya, Y. Wang, J. H. Fain, C. F. Archuleta, A. T. O'Neill and J. M. Desimone, *Adv. Mater.*, 2013, **25**, 5060-5066.

219    Y. Peng, Y. He, S. Yang, S. Ben, M. Cao, K. Li, K. Liu and L. Jiang, *Adv. Funct. Mater.*, 2015, **25**, 5967-5971.

220    S. P. Sullivan, N. Murthy and M. R. Prausnitz, *Adv. Mater.*, 2008, **20**, 933-938.

221    T. Xu, Y. Lin, M. Zhang, W. Shi and Y. Zheng, *ACS Nano*, 2016, **10**, 10681-10688.

222    Y. Chen, Q. Xiang, Z. Li, Y. Wang, Y. Meng and H. Duan, *Nano Lett.*, 2016, **16**, 3253-3259.

223    H. Yang, H. Zhu, M. M. Hendrix, N. J. Lousberg, G. de With, A. C. Esteves and J. H. Xin, *Adv. Mater.*, 2013, **25**, 1150-1154.

224    X. Yang, X. Liu, Y. Lu, J. Song, S. Huang, S. Zhou, Z. Jin and W. Xu, *J. Phys. Chem. C*, 2016, **120**, 7233-7240.

225    H. Liu, Y. D. Wang, J. Y. Huang, Z. Chen, G. Q. Chen and Y. K. Lai, *Adv. Funct. Mater.*, 2018, **28**, 1707415.

226    L. Zhang, J. Wu, M. N. Hedhili, X. Yang and P. Wang, *J. Mater. Chem. A*, 2015, **3**, 2844-2852.

227    M. Ge, C. Cao, J. Huang, X. Zhang, Y. Tang, X. Zhou, K. Zhang, Z. Chen and Y. Lai, *Nanoscale Horiz.*, 2018, **3**, 235-260.

228    S. Li, J. Huang, M. Ge, C. Cao, S. Deng, S. Zhang, G. Chen, K. Zhang, S. S. Al-Deyab and Y. Lai, *Adv. Mater. Interfaces*, 2015, **2**, 1500220.

229    C. Cao, M. Ge, J. Huang, S. Li, S. Deng, S. Zhang, Z. Chen, K. Zhang, S. S. Al-Deyab and Y. Lai, *J. Mater. Chem. A*, 2016, **4**, 12179-12187.

230    S. Gao, X. Dong, J. Huang, S. Li, Y. Li, Z. Chen and Y. Lai, *Chem. Eng. J.*, 2018, **333**, 621-629.

231    H. Liu, J. Huang, Z. Chen, G. Chen, K.-Q. Zhang, S. S. Al-Deyab and Y. Lai, *Chem. Eng. J.*, 2017, **330**, 26-35.

232    Y. Cheng, T. X. Zhu, S. H. Li, J. Huang, J. J. Mao, H. Yang, S. W. Gao, Z. Chen and Y. Lai, *Chem. Eng. J.*, 2019, **355**, 290-298.

**ARTICLE**

**TOC:**